Master’s Thesis

Insights into the turbulence structure and microphysical properties of "dusty cirrus" from lidar-radar synergies

University of Leipzig

Faculty of Physics and Earth Sciences

A thesis submitted in partial fulfillment of the requirements for the degree of

M. Sc. Meteorology

Submitted by:

Lukas Pieper, B. Sc.

Matriculation number: *******

1st August 2025

Supervisors:

Prof. Dr. Heike Kalesse-Los, Leipzig Institute for Meteorology, University of Leipzig

Prof. Dr. Andreas Macke, Leibniz Institute for Tropospheric Research (TROPOS)

Statutory Declaration

I hereby assure, that I created the presented work without unacceptable help from third parties and without the use of tools other than those indicated; thoughts directly or indirectly taken from foreign sources are acknowledged as such.

Leipzig,

Eidesstattliche Erklärung

Hiermit versichere ich, dass ich die vorliegende Arbeit ohne unzulässige Hilfe Dritter und ohne Benutzung anderer als der angegebenen Hilfsmittel angefertigt habe; die aus fremden Quellen direkt oder indirekt übernommenen Gedanken sind als solche kenntlich gemacht.

Leipzig,

Contents

1 Introduction

Clouds and aerosols play a key role in regulating the energy budget of our planet. While both can trap terrestrial long-wave radiation, contributing to a warming of the atmosphere, clouds also reflect incoming short-wave radiation, producing a cooling effect. Aerosols further influence this balance by modifying the microphysical properties of clouds, increasing cloud lifetime and albedo (Intergovernmental Panel On Climate Change 2023). The IPCC Report (Intergovernmental Panel On Climate Change 2023) predicted that changes to clouds due to anthropogenic emissions will have an overall warming effect on the future climate system. Radiative effects of cirrus clouds are suspected to cause significant climate forcing. In addition, aerosol-cloud interactions (ACI) influence the formation mechanisms and microphysical properties of cirrus clouds. Aerosols can serve as cloud condensation nuclei (CCN) or ice nucleating particles (INP), influencing droplet and ice formation pathways, respectively (Pruppacher and Klett 1997). Ice formation in cirrus clouds can occur either homogeneously, by freezing of a supercooled solution droplet or heterogeneously, via the presence INP's (Hoose and Möhler 2012; Pruppacher and Klett 1997). The dominant ice formation pathways have been shown to effects lifetime and radiative properties of cirrus clouds (Ansmann et al. 2019; Kuebbeler et al. 2014).

Due to its complexity, the relationship between aerosols and cirrus cloud microphysics remains poorly understood (Kärcher et al. 2022). In a review paper about the response of cirrus clouds to anthropogenic activities, Kärcher (2017) defined two dominant factors that constrain the ability of climate models accurately simulate cirrus formation: small scale variabilities in atmospheric dynamics and the ability of aerosols to act as INP. According to the author, uncertainties regarding the influence of these processes on cirrus formation need to be addressed in order to accurately estimate the effect of anthropogenic influences on cirrus clouds. In recent years, several studies have been published which explore the effects of aerosols on cirrus clouds.

Kärcher (2018) demonstrated, how soot particles emitted by aircrafts contribute to the formation of condensation trail cirrus (contrail cirrus) which generally enhance the radiative forcing on the climate system. In an analysis of radar and lidar observations from the MOSAiC campaign, Ansmann et al. (2025) found that high concentrations of aged Siberian wildfire smoke had a significant influence on heterogeneous cirrus formation in the arctic during the winter of 2019-2020 despite being rather inefficient INP. As an example of how ACI can be used to reduce global warming, the IPCC Report (Intergovernmental Panel On Climate Change 2023) suggested further investigation of techniques like Cirrus Cloud Thinning (CCT). As heterogeneous ice nucleation on INP has been observed to increase the size of ice crystals and decrease number concentrations, seeding cirrus clouds with INP is expected to decrease optical thickness of the clouds, thereby reducing the amount of thermal radiation that is trapped in the atmosphere by cirrus clouds (Mitchell and Finnegan 2009).

The so-called “dusty-cirrus” phenomenon is a great demonstration of aerosol-cloud interaction effects on cirrus formation and their incomplete representation in models. At least once per year, an extended cirrus cloud deck coinciding with a Saharan dust plume can be observed over Europe (Seifert et al. 2023). These clouds are typically characterized by their small scale convective structure (Kollath 2010). Contrary to the observation, that heterogeneous nucleation generally leads to fewer and larger ice crystals (Kuebbeler et al. 2014), Ansmann et al. (2019) have found in an INP – ICNC (Ice Crystal Number Concentration) closure study using lidar radar synergies, that dusty cirrus shows comparably high ICNC as well as small ice crystals. The fact that operational Numerical Weather Prediction (NWP) models so far have not managed to accurately depict these dusty cirrus events shows, that the parametrization of aerosol-cloud interactions is still lacking accuracy (Griesche 2016; Seifert et al. 2023; Weger et al. 2018). Enhanced understanding of the dusty cirrus phenomenon is not only crucial for improved accuracy of cloud cover predictions and thus enables better planning of solar energy production. These dusty cirrus events also provide opportunities to explore the effects of mineral dust on cirrus formation and the respective microphysical properties and the influence of dust aerosol on atmospheric dynamics. Although several studies have investigated dusty cirrus using model data, an analysis using height-resolved ground-based remote sensing is still lacking. This in turn would be a crucial step for the improvement of NWP models and ice nucleation parametrization.

The goal of this master’s thesis is to explore the turbulence structure and microphysical properties of dusty cirrus cloud decks. To this end, continuous measurements from the ACTRIS – Cloudnet station at Schneefernerhaus for the year 2022 are evaluated using a lidar-radar synergy approach described by Hogan and O’Connor (2004) and Tukiainen et al. (2020). Cloud observations are further compared to simulated dust concentrations from the EAC4 (ECMWF Atmospheric Composition 4) Global Reanalysis product provided by the Copernicus Atmosphere Monitoring Service (CAMS), to investigate a possible connection between dust and turbulence in cirrus clouds. The atmospheric conditions needed for dusty cirrus are explored with a focus on the mechanisms that lead to the formation of these events. Finally, the influence of wind shear on the observed turbulence structure is evaluated.

The thesis is structured as follows: in Chapter 2, current research on the effects of mineral dust aerosol on atmospheric parameters (sect 2.1 and 2.2) as well as the general characteristics and formation mechanisms of dusty cirrus (sect 2.3 to 2.5) is presented. Chapter 3 outlines the research questions of this thesis. Chapter 4 gives a detailed introduction to the methods and instrumentation employed in this study, with sect 4.1 and 4.2 providing descriptions of the models and instruments respectively. Sections 4.3 to 4.6 describe the retrieval processes for the necessary parameters. Chapter 5 investigates the statistical correlation between dust and turbulence, along with the influence of various atmospheric parameters on the formation of dusty cirrus, based on the results of model data and observations described earlier. Finally, Chapter 6 concludes with an attempt to answer the research questions and provide an outlook on possible future research directions.

2 Dusty Cirrus

Dusty cirrus events remain challenging atmospheric phenomena and are still underrepresented in most numerical weather prediction (NWP) models. Their formation and impacts are governed by an interplay of microphysical and dynamical processes. A key aspect is the effect of mineral dust aerosol on atmospheric radiation and cloud microphysics, which influences both cloud properties and atmospheric thermo-dynamics. Additionally, it is essential to consider the synoptic-scale conditions that facilitate the enhanced transport of Saharan dust into the upper troposphere over Central Europe, thereby creating favorable environments for the development of dusty cirrus clouds. Sections 2.1 and 2.2 provide an overview of the effects of mineral dust on atmospheric parameters, establishing a foundation for understanding how mineral dust can influence cirrus cloud formation. Sections 2.3 to 2.5 provide a general characterization of dusty cirrus properties and describe the synoptic conditions that facilitate their development.

2.1 Aerosol-Cloud Interaction (ACI)

While the effect of aerosols on liquid and mixed-phase clouds have been thoroughly explored, the effects on ice clouds are still rather poorly understood (*Climate Change 2013 – The Physical Science Basis* 2014).

Seifert et al. (2023) as well as Weger et al. (2018) have found in their simulation studies that the direct radiative effects of mineral dust in the atmosphere are neglectable in the presence of dusty cirrus formation. They attribute much larger importance to the effects of mineral dust on Aerosol-Cloud Interaction (ACI) through heterogeneous nucleation — a special pathway of ice formation, as will be outlined further below.

Ice nucleation

Water will freeze homogeneously at temperatures below −38°C and saturation ratios with respect to ice S_i = 1.4–1.7 (Pruppacher and Klett 1997). These atmospheric conditions can usually only be reached under rapid cooling conditions, as for example induced by orographic lifting (Kärcher and Lohmann 2003). Ice formation in clouds observed at higher temperatures or lower supersaturations must therefore be formed through heterogeneous nucleation (Seifert et al. 2003).

While homogeneous freezing has traditionally been regarded as the primary cirrus formation mechanism, this can in part be attributed to a lack of detailed observational data (Kärcher and Lohmann 2003; Lynch 2002). Recent studies have shown that ice formation is likely subject to a competition between heterogeneous freezing on INPs and homogeneous freezing of solution droplets, as homogeneous nucleation requires much higher supersaturation (Ansmann et al. 2025; DeMott et al. 1997; Kärcher et al. 2022). Heterogeneous nucleation can take place at temperatures below 0 °C and saturation ratios with respect to ice higher than 1 (Pruppacher and Klett 1997) and is likely to compete with or even prevent homogeneous nucleation by scavenging humidity from the air before the homogeneous freezing threshold is reached (Kärcher and Lohmann 2003).

Mineral dust's ability to serve as Ice Nucleating Particle (INP) in particular, has been well documented by several laboratory studies researching the role of aerosol particles for heterogeneous ice formation in the atmosphere (Hoose and Möhler 2012; Koehler et al. 2010). Several factors are critically influencing the nucleation ability of an aerosol particle. Mineral dust for example can serve as good INP due to its mineralogy, large size/surface area, insolubility and the crystallographic structure of the clay minerals (illite, montmorillonite, kaolinite) it contains (Pruppacher and Klett 1997). Due to these factors, mineral dust has been observed to initiate heterogeneous ice formation at a variety of different onset temperatures and saturation ratios.

Figure 1, extracted from Hoose and Möhler (2012) provides an overview of laboratory experiments assessing the ice nucleating abilities of different aerosols. The authors have found that super-micron dust particles can already nucleate ice at temperatures around $T = -10$ °C and saturation ratios of $S_\mathrm{i} \geq 1$. Submicron dust particles, which constitute the majority of mineral dust aerosols, can serve as INP at a wide range of temperature between −10 °C and −60 °C as well as saturation ratios of $S_\mathrm{i} \geq 1.2$, above and below water saturation.

Nucleation Modes

The high variability of nucleation onset conditions for mineral dust can be explained in part by its morphology, coatings, surface area and by the multiple modes of nucleation available.

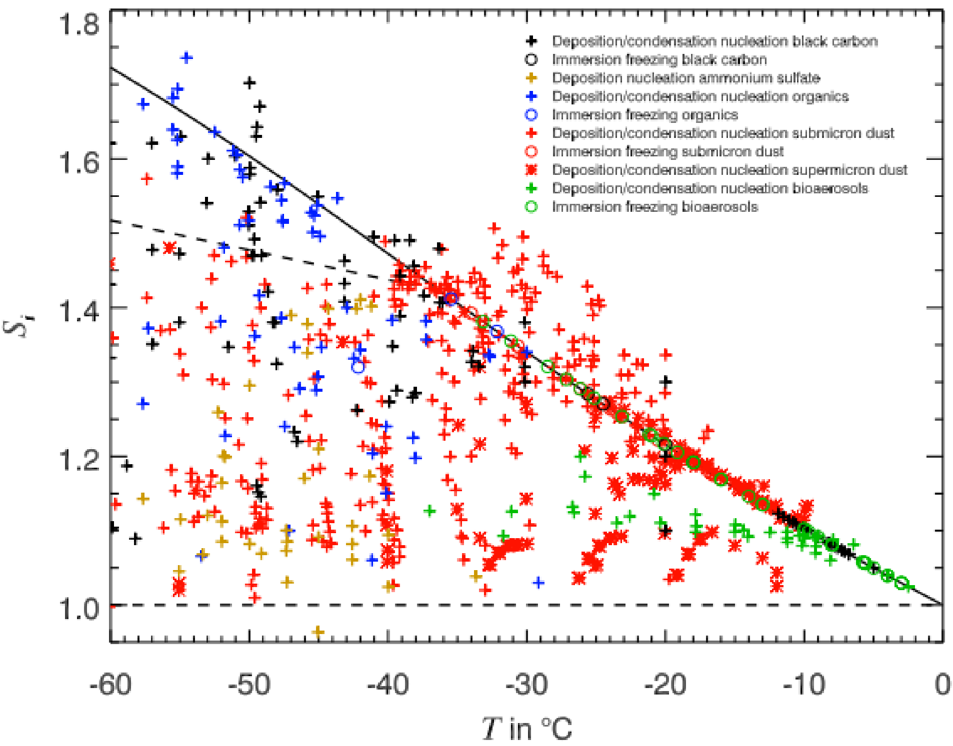

Figure 1, Onset conditions for ice nucleation of different aerosol particles by Hoose and Möhler (2012).

Figure 2 provides a summary of the 7 primary modes of ice nucleation. Four modes of heterogeneous ice nucleation are commonly defined in literature (Pruppacher and Klett 1997) and also shown in Fig. 2. *Immersion freezing* describes the freezing of a water droplet which has previously formed around a Cloud Condensation Nuclei (CCN). In this case the INP, which is already immersed in the droplet, initiates the nucleation process once sufficient temperatures are reached. This is considered to be the most common nucleation mode (Hoose and Möhler 2012). *Deposition nucleation* is characterized by the direct deposition of water vapor on the surface of an INP without going through the liquid phase. Some studies debate this mechanism and propose that deposition nucleation is instead a result of condensation in pores and subsequent freezing (pore condensation freezing — PCF) even below water saturation (David et al. 2019). *Condensation nucleation* is the formation of a water drop on the surface of CCN and subsequent freezing. In *contact nucleation* supercooled liquid water drops freeze at contact with an aerosol particle, because the contact provides the necessary activation energy to initiate a transition from liquid to solid phase.

Nucleation Parametrization

To be able to simulate aerosol cloud interaction, parametrizations are needed to simplify cloud microphysics and therefore make them computationally effective. In the case of cirrus

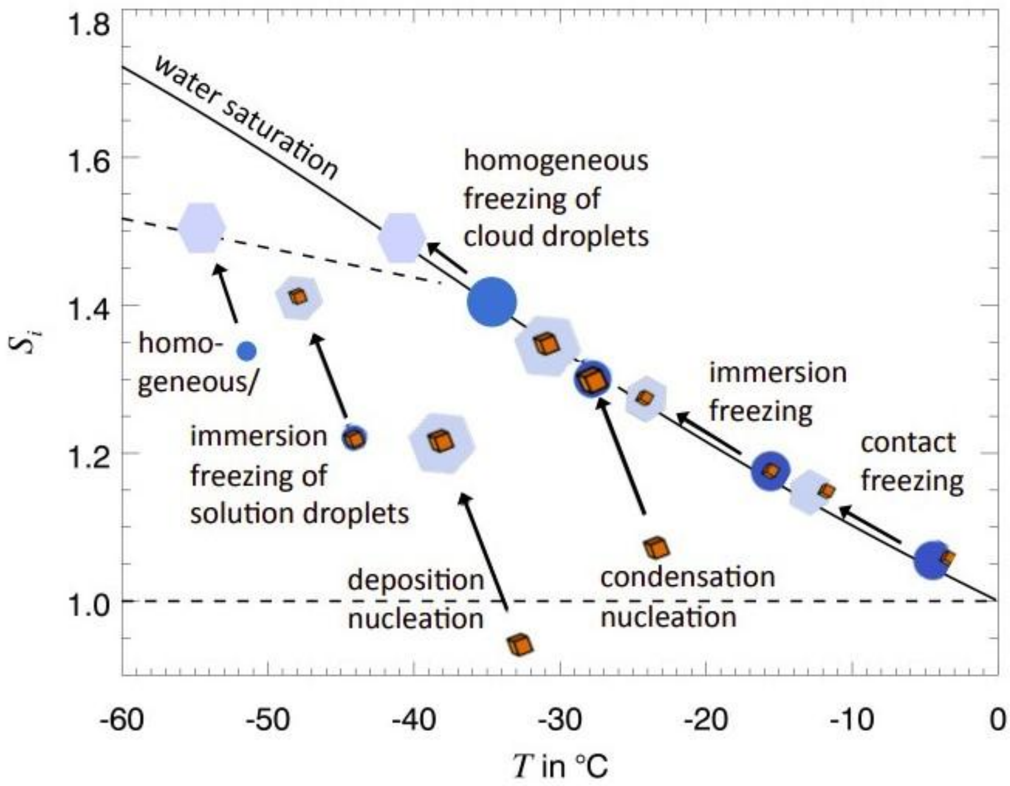

Figure 2, Nucleation modes and their respective temperature and saturation ratio ranges by Hoose and Möhler (2012).

clouds, the formation mechanisms are rather complex and still poorly understood. Ice nucleation can either happen homogeneously at temperatures below −38 °C and supersaturation ratios of S_i = 1.4–1.7 (Kärcher and Lohmann 2003; Pruppacher and Klett 1997) or heterogeneously at temperatures below 0 °C and $S_i > 1$.

High updraft velocities, leading to high cooling rates are typically required to reach the relatively high saturation ratios required for homogeneous nucleation. Kärcher et al. (2006) therefore developed a parametrization which can estimate the number density and size of ice crystals in a cirrus cloud as a function of vertical velocity, temperature and saturation ratio. Aerosol number concentration and preexisting cloud ice are allowed to compete for ice nucleation, thereby decreasing the number of homogeneously formed ice crystals. A similar model has recently been developed by Ansmann et al. (2025).

The parametrization of heterogeneous nucleation is somewhat more complex. Besides the 4 described ice formation pathways, also the atmospheric conditions needed for heterogeneous nucleation vary strongly depending on aerosol composition, size, shape and coatings. Parametrizations of heterogeneous nucleation are commonly attributed to one of two approaches. *Deterministic* parametrizations (Phillips et al. 2008; Ullrich et al. 2017) commonly depend on physical properties of the aerosol (shape, size, surface area, chemical composition) as well as atmospheric conditions (temperature, saturation ratio). The *stochastic* approach is based on classical nucleation theory (CNT) and includes a dependence on time. Particle properties in both approaches are determined in laboratory studies and then quantified with the nucleation rate coefficient J_{het} (stochastic) or for example the active surface site density n_s (*deterministic*). In contrast to the stochastic approaches, deterministic approaches require less complex input parameters and are therefore easier to apply (Burrows et al. 2022).

A model study performed by (Ansmann et al. 2025) and based on radar and lidar observations during the MOSAiC (Multidisciplinary drifting Observatory for the Study of Arctic Climate) campaign, compared the two ice formation pathways with regard to their required atmospheric conditions (updraft, temperature, relative humidity and INP concentrations). This study underlines that in the presence of even inefficient INPs like smoke aerosol, heterogeneous nucleation still remains the more likely ice formation pathway. In the simulation, INP concentrations retrieved from lidar measurements before and after cirrus events in the Arctic winter 2019 – 2020 were used as input parameters to analyze if the observed ICNC can be reproduced solely through heterogeneous nucleation. The authors simulated the adiabatic ascent of a smoke-filled air parcel starting from the top of the cirrus cloud, using meteorological input parameters from MOSAiC observations. For the ascent of the air parcel, typical updraft velocities for large-scale lofting as well as lofting through gravity waves were used and the water vapor mixing ratio was held constant, so that lofting resulted in an increase of the ice saturation ratio. Their ice nucleation parametrization followed an approach based on classical nucleation theory (CNT). They also assumed that all smoke particles with a radius > 250 nm can serve as potential INP and that there was an unlimited reservoir of stratospheric smoke aerosol in this particular case. Figure 3 shows an example of simulation results for a gravity wave with an amplitude of 250 m at an updraft velocity of 0.2 m/s. A burst of heterogeneous ice nucleation was simulated at a moderate lofting of below 200 m while homogeneous lofting under these conditions required a lofting of more than 200 m. Reducing the amplitude of the updraft led to ICNC values much closer to observations from the MOSAiC campaign, with low ICNC for heterogeneously formed ice crystals and a complete suppression of homogeneous nucleation. Finally, they argue that shallow updrafts with low amplitudes and velocities were much more common during MOSAiC, making heterogeneous ice nucleation on aged

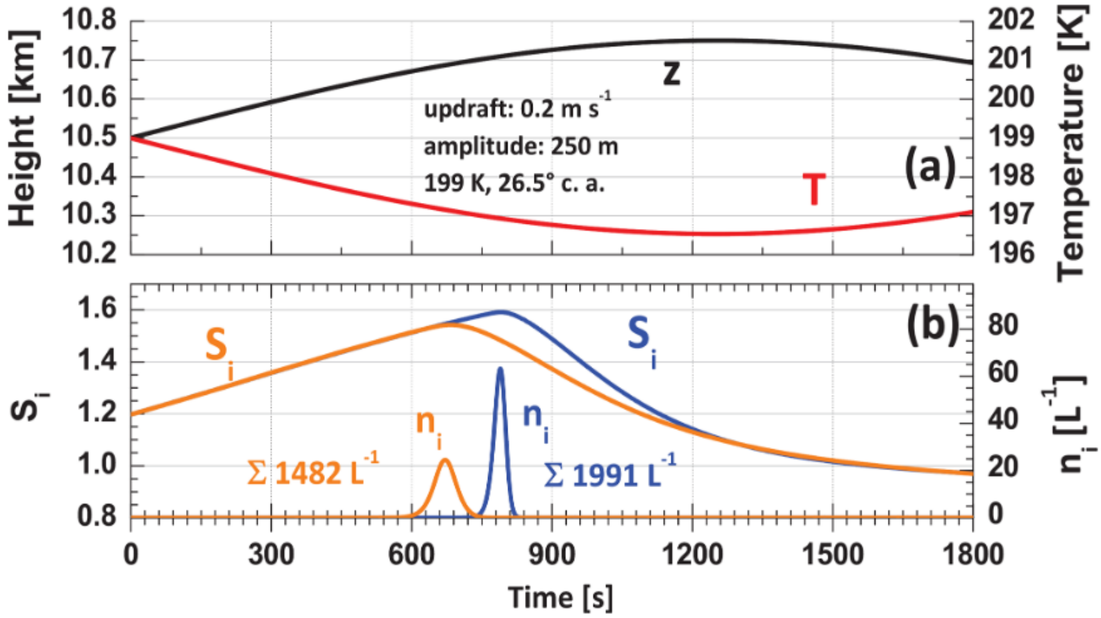

Figure 3, Simulation of heterogeneous (orange) and homogeneous (blue) ice nucleation with meteorological conditions observed at cirrus events in Arctic winter 2019 – 2020 (b) and updraft velocity and amplitude of gravity waves (a). Taken from Asmann et al. (2025).

smoke aerosol a likely ice formation pathway at a supersaturation S_i of ~ 1.5. In contrast to smoke aerosol, mineral dust is a rather efficient INP and can trigger ice formation at supersaturations of $S_i \approx 1.2$.

Weger et al. (2018) simulated a Saharan dust event in April 2014 over Germany and compared different INP parametrizations. They have found the parametrization of Ullrich et al. (2017) to provide more accurate results regarding cirrus formation than previous parametrizations with similar approaches, e.g. Phillips et al. (2008).

The deterministic ice nucleation parametrization by Ullrich et al. (2017) assumes that the nucleation ability of an aerosol particle is approximately proportional to its surface area density. The nucleation efficiency of an aerosol species is quantified with the ice nucleation active surface site (INAS) density n_s. The INAS density can be calculated by dividing the ice number concentration n_i by the total aerosol surface area concentration s_ae which is calculated by the aerosol number concentration n_{ae} times the aerosol surface area S_{ae}. It has been empirically retrieved from laboratory measurements in the Aerosol Interaction and Dynamics in the Atmosphere (AIDA) cloud chamber a Karlsruhe Institute for Meteorology (KIT).

(1) **INAS density calculation**: $n_\mathrm{s}(T, S_\mathrm{i}) \approx \frac{n_\mathrm{i}(T, S_\mathrm{i})}{n_\mathrm{ae} S_\mathrm{ae}} = \frac{n_\mathrm{i}(T, S_\mathrm{i})}{s_\mathrm{ae}}$

Ullrich et al. (2017) assume that freezing of supercooled droplets is approximately time independent and ice germs are formed on “active sites” of particles which can have soluble coatings, pores, cavities or other prerequisites that favor ice nucleation. The parametrization accounts for the effects of immersion freezing and deposition nucleation in the formation of cirrus clouds. These two modes are believed to be the dominant nucleation modes for mineral dust particles (Burrows et al. 2022) especially at cirrus regimes. While there is a strong dependence of immersion freezing on temperature, deposition nucleation on desert dust is observed to have a high dependence on saturation ratio as well as temperature. In their laboratory measurements Ullrich et al. (2017) could not find a large difference in INAS density between different samples of desert dust. They conclude that their parametrization can accurately depict INAS densities for immersion freezing of freshly emitted as well as aged dust particles. INAS density results for deposition nucleation come with a somewhat higher error of several orders of magnitude due to the uncertainty regarding its formation mechanisms (Hoose and Möhler 2012).

2.2 Aerosol Radiation Interaction (ARI)

Aerosols can directly interact with radiation through scattering and in some cases absorption processes, thereby influencing the net radiation at the top of atmosphere (TOA). Dust layers make the atmosphere opaquer and can “reflect” shortwave radiation back to space as well as “trap” longwave radiation in the atmosphere. The scattering of shortwave and longwave radiation of aerosols strongly depends on particle size and dust composition. Dust layers have been observed to cause net cooling of the surface in daytime because shortwave reflection on submicron dust particles dominates over longwave trapping (Choobari et al. 2014). However, a nighttime warming of the surface has been proposed due to the absence of shortwave radiation (Hansell et al. 2010). The IPCC Report (Intergovernmental Panel On Climate Change 2023) estimates a radiative forcing (RF) through *ARI* caused by anthropogenic aerosol of $-0{,}22$ Wm^2. While most aerosols have a negative RF, black carbon shows the highest absorption capabilities and creates an additional RF through deposition on snow.

2.3 Dusty cirrus characterization

Dusty cirrus clouds are characterized as an extended cirrus cloud deck with a shallow convective structure like that of a stratocumulus shield. Dusty cirrus can best be observed in satellite images of the early morning (see Fig. 4). A slow rate of disappearance over the course of the day was reported, as well (Kollath 2010). This cloud structure usually appears as a result of a northward transport of dust-infused North African airmasses. However, similar dusty cirrus cloud decks were observed over East-Asia and are probably caused by dust transport from the Gobi Desert (Zeng et al. 2023). While not every dust event necessarily produces a dusty cirrus, Seifert et al. (2023) have called dusty cirrus "…the dominant aerosol–cloud–radiative effect of mineral dust over Europe."

In a modeling study using the ECHAM5-HAM general circulation model, Kuebbeler et al. (2014) found that cirrus clouds which are primarily formed through heterogeneous nucleation under normal dust conditions typically have fewer and larger ice crystals compared to homogenously formed cirrus. In contrast, dusty cirrus has been observed to have rather high ice crystal number concentrations with small crystals at cloud top, leading to an extended cloud lifetime (Ansmann et al. 2019) as well as an increased cloud albedo and reflection of shortwave radiation.

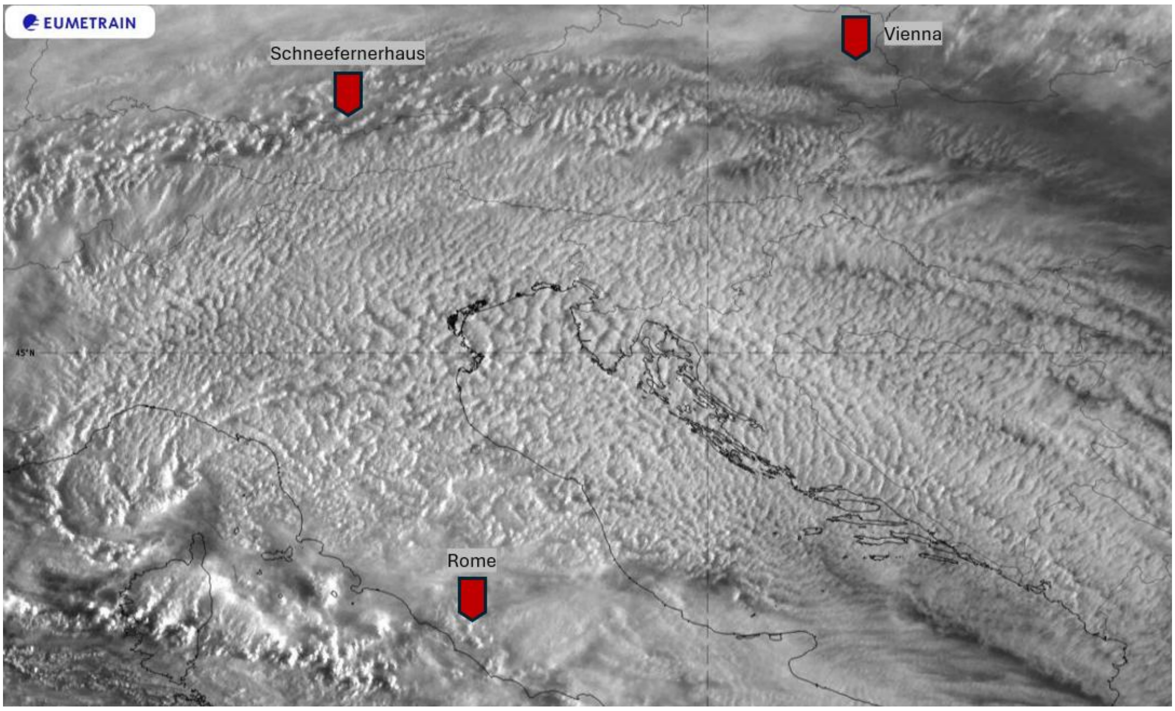

Figure 4, High-resolution visible image from MSG SEVIRI over the northern Mediterranean region on 30 March 2022 at 0600 UTC, showing an extended dusty cirrus cloud deck with the typical convective structure. Adapted from: https://resources.eumetrain.org/satmanu/CMs/DIBS/navmenu.php?page=1.0.0 (access: 11.06.2024).

2.4 Dusty cirrus formation

Dust-Infused Baroclinic Storms (DIBS)

The synoptic event commonly associated with dusty cirrus formation was termed dust-infused baroclinic storm by Fromm et al. (2016). DIBS can be described as far southward reaching midlatitude cyclones with high surface windspeeds, entraining dust from desert regions of North Africa, Mongolia or China. Warm Conveyor Belts (WCB) at the frontal regions of the storm subsequently serve to transport dust masses northward and to upper tropospheric levels. Dust particles can subsequently act as INP once the atmospheric conditions for heterogeneous ice nucleation are met. This mechanism can lead to the formation of optically thick and extended cirrus cloud decks with an unusually long lifetime (Seifert et al. 2023).

Nighttime radiative cooling theory

In recent years two theories have been proposed regarding the formation of dusty cirrus. According to Kollath (2010), longwave radiative cooling through the night leads to baroclinic instability within the cloud (see Figure 5). This in turn causes shallow convection, leading to the typical cellular structure of dusty cirrus clouds. Increased short wave absorption in the daytime leads to a more stable stratification, which explains why the cellular structure is most visible in the morning and disappears towards the afternoon.

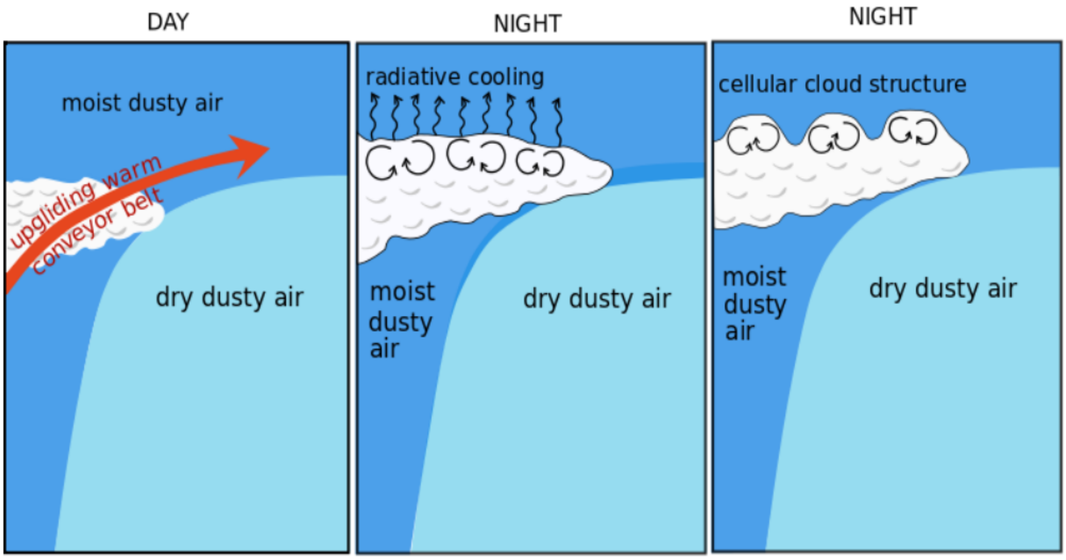

Figure 5, Schematic, showing the formation of dusty cirrus according to the nighttime radiative cooling theory of Nagy & Kollath (2010).

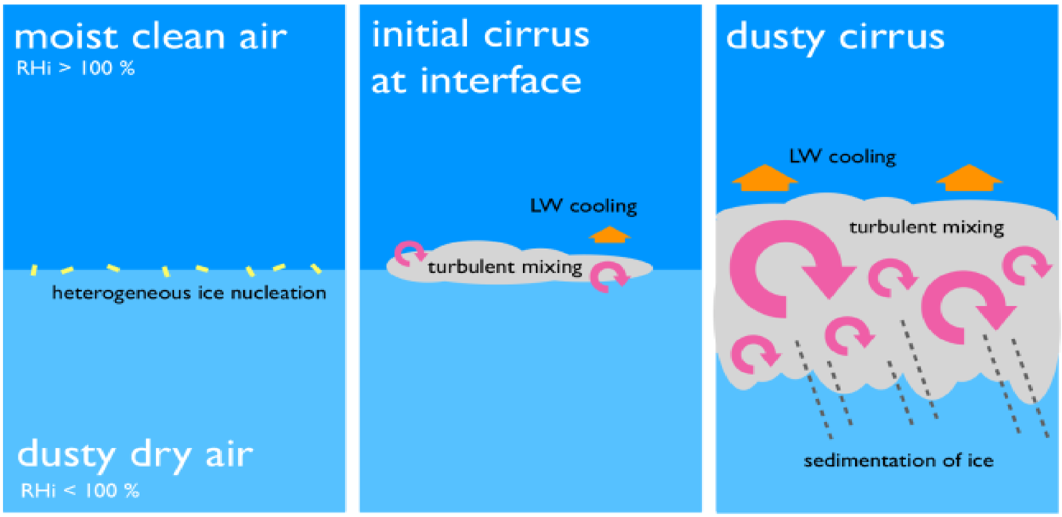

Figure 6, Schematic, showing the formation of dusty cirrus according to mixing instability theory of Seifert et al. (2023).

Mixing-instability theory

Seifert et al. (2023) favor a different theory, which is more aligned with their assumption, that dusty cirrus formation is initiated above and not within the dust layer. According to them, the cirrus formation is caused by a mixing instability between a moist clean air layer above a dry dusty layer. Heterogeneous nucleation caused by gravity waves or shear-induced clear air turbulence at the interface of these separate layers leads to an initial cirrus formation. Longwave cooling at the top of the initial cirrus will then cause a local destabilization of the atmosphere. Turbulent mixing at the interface subsequently entrains dust aerosol into the moist layer, thickening the initial cirrus cloud (see Fig. 6).

3. Research Questions

Based on the presented theoretical background of dusty cirrus and their atmospheric implications, several research questions emerge that will be addressed in the course of this thesis:

1. Do turbulent cirrus clouds also appear under dust-free conditions, or is turbulence a characteristic exclusive to cirrus under dust-laden conditions?

One of the most prominent characteristics of dusty cirrus cloud decks is the cellular structure that can be observed in satellite images (Kollath 2010; Seifert et al. 2023). Kollath (2010) attributes the convective structure to nighttime radiative cooling at the top of the cirrus cloud layer, which leads to a destabilization of the cloud layer and thus creates small-scale convection within the cloud. A similar theory was proposed by Fusina and Spichtinger (2010) when investigating the relationship between cirrus clouds and radiation in a modelling study. They conclude, that in case of supersaturated air layers, radiative cooling can lead to small scale turbulence and subsequently initialize ice nucleation when reaching sufficiently large lofting amplitudes. While small scale lofting has been shown to be sufficient to initiate heterogeneous nucleation (Ansmann et al. 2025; Spichtinger 2014), and these turbulences might significantly influence cirrus formation. The correlation between dust and turbulence has not been sufficiently explored so far. Hence, a statistical long-term analysis will be performed to assess the relationship between the appearance of dust and cirrus turbulence.

2. Do the proposed dusty cirrus formation mechanisms agree with state-of-the-art height-resolved observations and models?

Kollath (2010) proposes nighttime radiative cooling as the key driver of dusty cirrus formation. The author argues that high dust aerosol concentrations at cirrus cloud level lead to an increase in outgoing longwave radiation and radiative cooling during nighttime conditions. This in turn leads to a destabilization of the layer, resulting in shallow convection. In contrast, an aerosol induced increased absorption of short-wave radiation during daytime, leads to more stable stratification, thereby dissolving the turbulent structure of the dusty cirrus over the course of the day. This theory is largely based on 2-D satellite images. Thus, ground-based height-resolved remote sensing will be used to assess the proposed increase of turbulence during the night and decrease in daytime.

Seifert et al. (2023) proposed that the cirrus formation is initiated at the interface of a dry dusty air layer and a supersaturated dust-free air layer above. Lofting though gravity waves or shear induced turbulence lead to initial cirrus formation though heterogeneous nucleation. Longwave radiative cooling at the top of the initial cirrus then leads to destabilization and convective overturning within the cirrus layer. In contrast to this theory, Ansmann et al. (2019) found that the cirrus usually formed within the dust layer and not at the interface of two layers. Where the cirrus formation actually takes place will be investigated using a combination of model dust concentrations from CAMS and remote sensing observations from ACTRIS Cloudnet.

3. What are the atmospheric conditions necessary for "dusty cirrus" and does wind shear play a role in driving the observed turbulence?

The general atmospheric conditions leading to the formation of dusty cirrus, as well as the source of dusty cirrus turbulence are associated with large uncertainties. Seifert et al. (2023) propose that wind shear or gravity waves could be responsible for the initial lofting required for heterogeneous nucleation. In their approach to develop a sub-grid dusty cirrus parametrization, they set the minimum values for dusty cirrus formation to 50 µg/kg for dust concentration and S_i = 0.7 for the supersaturation with regard to ice. The low supersaturation threshold assumes that processes relevant for initial ice formation start much below model resolution. To evaluate these thresholds, typical dust concentrations and supersaturations surrounding dusty cirrus cloud decks as well as the influence of wind shear on cirrus turbulence will be studied.

4. What are possible reasons for model inaccuracies in the presence of Saharan dust?

Operational NWP models largely operate with background aerosol climatologies instead of explicitly modelling emission and transport of aerosols, leading to large discrepancies between modelled cloud cover and observations in the presence of Saharan dust (Griesche 2016). Seifert et al. (2023) and Weger et al. (2018) both point out, that even including aerosol cloud interaction schemes as well as aerosol emission and transport does not suffice to accurately model cloud cover at dust events. Weger et al. (2018) identified uncertainties in the ice nucleation properties of mineral dust as well as too low specific humidities at the altitude of the dusty cirrus as the main reasons for the models inaccuracy. Seifert et al. (2023) attributed the discrepancies between model and observations to the coarse vertical model resolution and therefore developed a sub-grid parametrization to improve the simulation of dusty cirrus. A comparison of Cloudnet model cloud cover and atmospheric parameters to radar observations of dusty cirrus clouds will be performed for several case studies to evaluate the forecast skill of ECMWF – IFS. Further, an approach by Ansmann et al. (2025) will be used to explore if sub-grid lofting would be sufficient to reach atmospheric conditions required for heterogeneous nucleation on mineral dust in cases where the model fails to simulate clouds in the presence of dust aerosol.

4. Methods and Instrumentation

Examples for the evaluation of Saharan dust events using height-resolved ground-based observations and NWP model data can be found in recent literature (Ansmann et al. 2019; Griesche 2016; Seifert et al. 2010; Weger et al. 2018).

Weger et al. (2018) performed a modeling study using the COSMO-MUSCAT model. The Consortium for small scale modelling (COSMO) is a non-hydrostatic regional NWP model online coupled to the chemistry transport model MUSCAT (MUltiScale Chemistry Aerosol Transport). They performed dusty cirrus simulations including emission and transport of aerosols and aerosol-cloud interaction scheme as well as an INP parametrization scheme of Ullrich et al. (2017). Comparing the model outputs to in situ and ground-based observational data, the authors found significant disparities which they primarily attribute to insufficiently realistic boundary conditions in their model.

Seifert et al. (2023) introduced a sub-grid dusty cirrus parametrization scheme into ICON – ART (ICOsahedral Nonhydrostatic model – Aerosol and Trace Gases) based on the mixing instability theory. The Aerosol and Reactive Trace gases (ART) module was developed at KIT to integrate aerosol and trace gas emissions, dynamics and chemical reactions into the ICON model as described in Rieger et al. (2015). The online coupled ICON-ART model can also simulate aerosol effects on radiation and cloud formation using the heterogeneous nucleation parametrization by Ullrich et al. (2017). Cirrus formation is triggered, at dust concentrations of 50 $\mu g\ kg^{-1}$, saturation ratios with respect to ice of 0.7 and a temperature lapse rate of 6.5 $K\ km^{-1}$ as a measure for atmospheric stability. The low saturation ratio threshold assumes that initial cirrus formation is triggered by turbulent structures well below model resolution. While the new parametrization greatly improved the forecast skill in the presence of Saharan dust when compared to cloud cover and cloud top height from MSG SEVIRI (Meteosat Second Generation – Spinning Enhanced Visible and Infrared Imager), an evaluation with height-resolved ground-based remote sensing has not been performed, yet.

Ansmann et al. (2019) have demonstrated how ground-based lidar measurements in combination with appropriate parametrization schemes can be used to deduce the ice nucleating particle number concentrations (INPC) from backscatter and depolarization ratio profiles. Additionally, they calculated ICNC values from a combination of lidar, cloud radar and modelling products. A decent agreement between INPC and ICNC values was found, leading to the conclusion that the observed dusty cirrus was a product of primarily heterogeneous ice formation. Bühl et al. (2019) and Ansmann et al. (2019) have both demonstrated, how to retrieve ICNC from a combination of terminal fall velocity, radar reflectivity factor and particle extinction coefficients measured with lidar and radar.

Griesche (2016) studied the effects of mineral dust on the forecast skill of NWP models by comparing operational model data to remote sensing observations in his master's thesis. Beside a substantial disagreement between models and observations, he highlighted a possible connection between turbulence and cirrus formation in dust-laden episodes. In a later study, Griesche et al. (2020) detailed a method to retrieve Eddy Dissipation Rates (as a measure of cloud turbulence) from Doppler radar measurements. The measurements were performed using the shipborne remote-sensing platform OCEANET on an Arctic cruise of the German research vessel Polarstern of the Alfred Wegener Institute (AWI) Bremerhaven.

In this Section, different methods and instruments will be introduced that provide information about the microphysical properties and turbulence structure of dusty cirrus clouds as well as the surrounding meteorological conditions. Based on these techniques, the research questions introduced in Chapter 3 will be addressed.

4.1 Ground-based Observations

Several approaches have been made to use height-resolved ground-based observation to obtain information about the effects of Saharan dust on cloud formation and microphysics (Ansmann et al. 2019; Ansmann et al. 2025; Griesche 2016; Seifert et al. 2010; Weger et al. 2018). A combination of lidar (light detection and ranging) and cloud radar (cloud radio detection and ranging) is the state-of-the-art approach for height-resolved remote sensing studies on aerosol-cloud interactions. Lidar products include backscatter and depolarization ratios and can provide valuable information about aerosol size, shape and concentration. Due to their relatively small wavelength in or near the visible spectrum, lidar signals tend to extinguish quickly once they start penetrating a liquid cloud. Hence, cloud radars, usually operated in the mm to cm wavelength regime are often used for in-cloud measurements. Cloud radar products can be used to obtain information about cloud cover, cloud structure, ice water content (IWC), cloud particle size and type and turbulence within the cloud. A combination of different products from both instruments is necessary to obtain full coverage of the troposphere. In this Chapter, the operational principles of lidar and cloud radar will be explained.

4.1.1 Polly^{NET}

Polly^{NET} is an international network of institutes employing portable multiwavelength-Raman-polarization lidars (Polly^{XT}) (Engelmann et al. 2016) which can be remotely operated and perform 24/7 cloud and aerosol observations. Measuring instruments in all participating institutes have a standardized design, to ensure consistent data quality and high comparability. Goal of the network is to contribute to a global aerosol climatology (Baars et al. 2016). Close-to-real time data from the remote sensing sites is provided at https://polly.tropos.de hosted by TROPOS.

Lidar (Light detection and ranging)

The simplified setup of a lidar (see fig. 7) contains a transmitter and a receiver. The transmitter consists of a laser which generates short light pulses which are emitted at a close-to-zenith angle into the atmosphere. In the receiver, backscattered light is collected by a telescope and subsequently analyzed for its intensity and polarization state. The collected information is then converted into an electrical signal to permit computer analysis

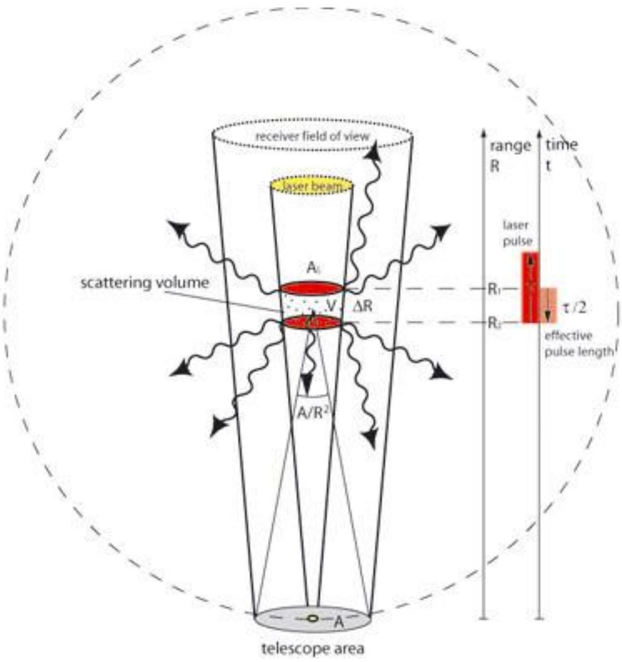

Figure 7, schematic of the lidar working principle, taken from https://www.tropos.de/forschung/grossprojekte-infrastruktur-technologie/technologie-am-tropos/fernerkundung/lidar (access: 27.07.2024).

(Wandinger 2005). Data analysis algorithms are then used interpret the received signal (Illingworth et al. 2007). Typical wavelengths for the detection of aerosol properties are, for example 355 nm, 532 nm and 1064 nm (Baars et al. 2016). The Polly^{XT} Raman lidars employed at Polly^{NET} can separate the received signal into contributions by molecule and particle contributions (Ansmann and Müller 2005). Ceilometers, simpler lidar systems which operate with reduced power, small telescope and only at single wavelengths, are often used as baseline lidar instruments at continuously operating remote sensing sites. While they don't provide details on the present aerosol types, they are valuable tools for observation of the cloud and aerosol structure at a site.

Retrieval of aerosol properties

In its most basic form, the detected signal of the instrument can be described as:

$$(2)\quad \boldsymbol{P(R) = K\, G(R)\, \beta(R)\, T(R).}$$

The first two variables are determined by the experimental setup. *K* describes a system constant, including the emitted energy of the laser pulse as well as its duration. The second variable *G(R)* consists of two parts: The overlap function, which accounts for geometric effects of the experimental setup on the measured signal, and the negative quadratic dependence of the strength of the received signal with distance *R* (Wandinger 2005).

The backscatter coefficient describes the amount of light that is reflected at distance *R* and a scattering angle of 180°. When determining the backscatter coefficient, it must be considered that the atmosphere contains a multitude of different molecules and particles with different scattering and absorption properties. Molecular scattering largely depends on the density of the atmosphere and therefore the meteorological conditions such as pressure and temperature. The scattering of aerosols is highly variable and depends on the aerosol type, shape, and size distribution as well as the wavelength of the laser pulse (Ansmann and Müller 2005).

Finally, a part of the emitted energy will be lost during the passage of the light pulse through the atmosphere. The transmission term *T(R)* describes the extinction of light, by absorption and scattering, on the way from the lidar to the location of the backscatter signal. Like the backscatter coefficient (see Fig. 8 for an example of a profile of attenuated backscatter at a dusty cirrus event), extinction by aerosols depend on a variety of particle properties (Wandinger 2005).

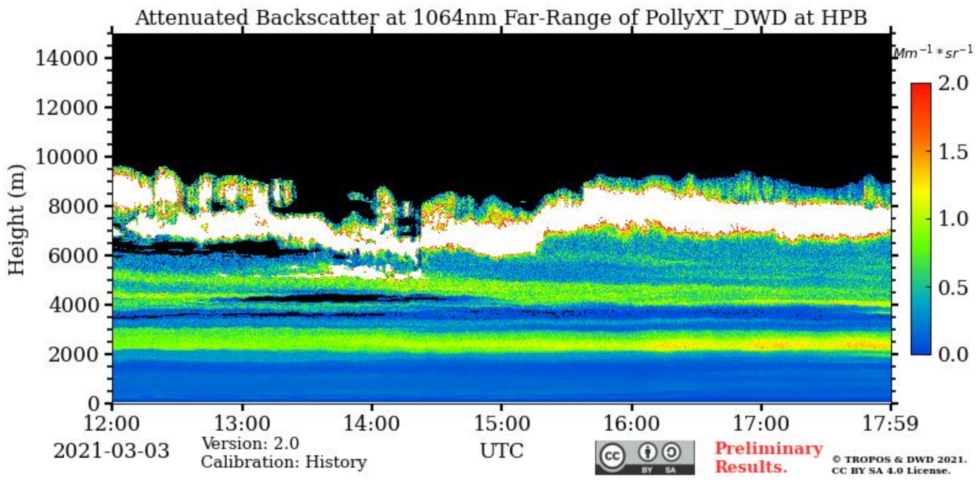

Figure 8, Time-height cross-section of attenuated backscatter coefficient at 1064 nm observed above Hohenpeißenberg on 3 March 2021, 1200–1400UTC. Shown is a dusty cirrus event with the cirrus at 6-10km height. Taken from Polly^{NET}

Aerosol types are characterized through their characteristic ratios of backscatter and extinction coefficient, the so-called lidar ratio.

(3) $\boldsymbol{L_{\mathrm{aer}}(R)} = \frac{\alpha_{\mathrm{aer}}(R)}{\beta_{\mathrm{aer}}(R)}$

The lidar ratio can be used for typing of the aerosol populations present in the atmosphere. Typical lidar ratios for, e.g., Saharan dust aerosols at 532 nm are 50–80 sr (Ansmann and Müller 2005). Polarization lidars typically produce and emit linearly polarized light due to the construction of the emitter. When light is scattered by a particle, it tends to change its state of polarization. The degree of depolarization upon scattering on a particle depends on the scattering properties or shape of the particle (see Fig. 9 for an example of a profile of the volume depolarization ratio at a dusty cirrus event). Spherical particles do not significantly change the state of polarization. Non-spherical particles, like dust or ice crystals on the other hand, can lead to high depolarization ratios (white layered area in Fig 9). To obtain information about the shape of the detected particles the depolarization ratio can be deduced by use of a polarizer close to the focal plane of the receiver of the lidar. For calibration, the polarizer is automatically rotated to +45 and -45 to the polarization plane of the laser several times per day. The volume depolarization ratio $\boldsymbol{\delta}$ can then be calculated from the ratio of the cross-polarized and the total signal $\boldsymbol{\delta'}$, the absolute calibration C and the total and cross-polarized receiver transmission ratios R_c and R_t (Engelmann et al. 2016):

(4) $\boldsymbol{\delta(V)} = \frac{1-\delta' / C}{\delta' R_t / C - R_c}$

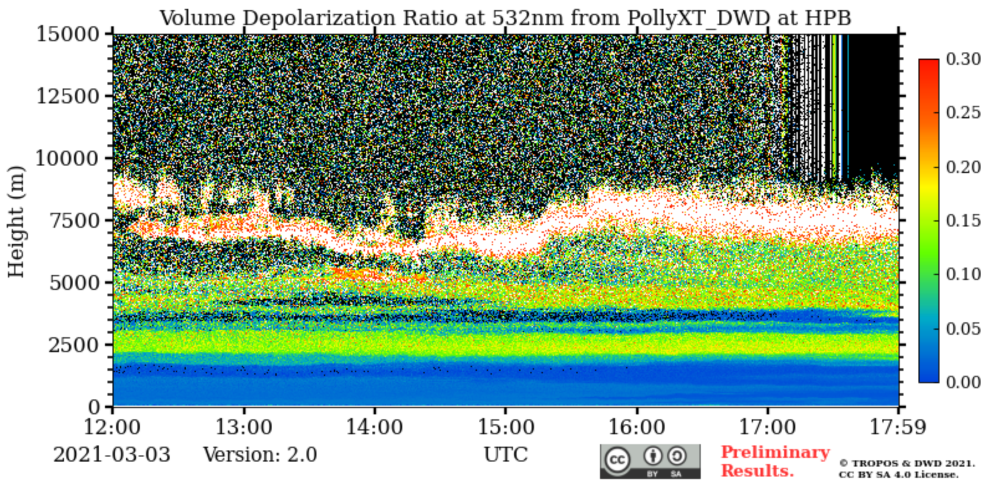

Figure 9, Time-height cross-section of the volume depolarization ratio at 532 nm observed above Hohenpeißenberg on 3 March 2021, 1200–1400UTC. Shown is a dusty cirrus event with the cirrus at 6-10 km height. Taken from Polly^{NET}

4.1.2 ACTRIS Cloudnet

Cloudnet, as part of ACTRIS (Aerosol, Clouds and Trace gases Research InfraStructure) is a pan-European network of ground-based remote sensing sites operated by different participating institutes. The original goal of the project was to provide standardized cloud observational data for the purpose of evaluating model simulations and improve NWP. The Cloudnet remote-sensing sites are equipped with a Doppler cloud radar, a ceilometer (lidar) and a microwave radiometer, running 24/7. The synergy of the instruments can be used to derive, e.g., ice cloud microphysics using algorithms developed by Cloudnet (Illingworth et al. 2007; Tukiainen et al. 2020). Cloudnet data is available at https://cloudnet.fmi.fi provided by the Finnish Meteorological Institute.

Cloud radar (Cloud Radio Detection and Ranging)

Cloud radars can be used to derive a variety of cloud and precipitation properties. The operation principle is similar to that of a lidar (see Fig. 10). They consist of a transmitter, an antenna, a receiver, a processing unit for the received signal and a computer analyzing the processed signal. Instead of a laser pulse, an electromagnetic pulse in the mm-range at a frequency of typically ~35 GHz (wavelength of ~0.8 cm) or 94 GHz (wavelength of ~ 3mm) is emitted by a directional antenna. The choice of frequency can be attributed to the fact that the higher frequency of a lidar will be more sensitive to smaller particles, leading to more attenuation in the detection of liquid cloud particles. The radar reflectivity (strength of the backscattered signal) can provide information about the presence, type and structure of clouds, with the drawback that small aerosols are hardly detectable. Doppler radars can

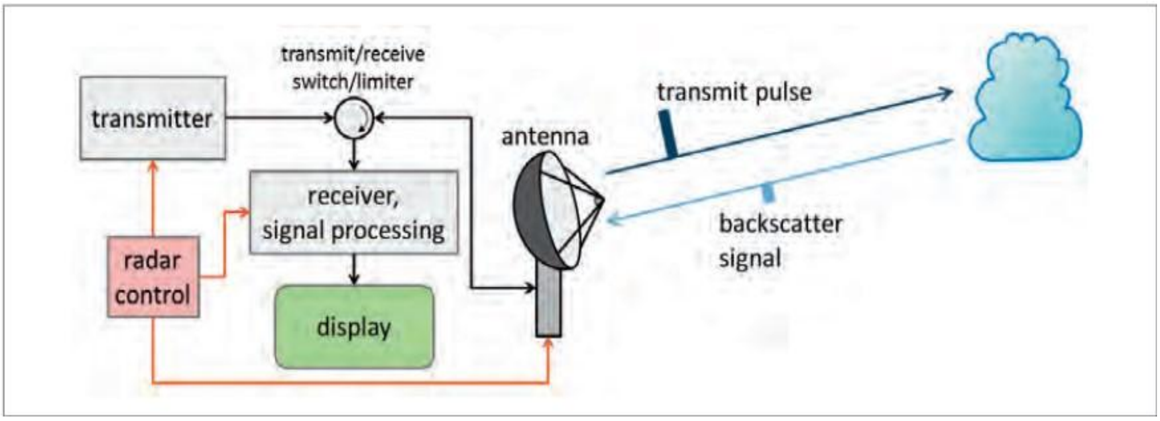

Figure 10, Working principle of a cloud radar. Taken from Hagen et al. (2022)

additionally derive up and downward motion of cloud particles relative to the instrument. Polarization radars can give information about shape and orientation of the detected cloud particles (Hagen et al. 2022).

Retrieval of cloud microphysical properties

The strength of the detected radar signal P_r can be described by (Fabry 2015):

$$(10)\ \boldsymbol{P_r} = \frac{1.22^2 0.55^2 10^{-18} \pi^7 c}{1024 \log_e 2} \frac{P_t \tau D_a^2}{\lambda^4} \frac{T(0,r)^2}{r^2} \|\boldsymbol{K}\|^2 \boldsymbol{Z}.$$

The first term of the equation contains a set of constants related to the characteristics of the observed volume and the beamwidth of the antenna as well as the speed of light c. The second term describes the setup of the radar with P_t being the power of the pulse, $\boldsymbol{\tau}$ the pulse duration, D_a the diameter of the antenna and λ the emitted wavelength. The third term includes attenuating effects of the atmosphere on the path to the observed volume. T is the transmittance of the atmosphere between the emitter and the observed volume at range r. The final term depends on the scattering properties of the target. $\|\boldsymbol{K}\|$ is the dielectric constant of the observed particles, a unitless quantity describing the scattering and absorption properties of the volume, with typical values for water drops about 0.93 and ice crystals 0.176 (Rauber and Nesbitt 2018). Z represents the radar reflectivity factor, a quantity which is frequently used to determine cloud and precipitations properties.

Most targets of radar observations are much smaller than the wavelength used (35GHz ~ λ = 0.8 cm). As a first approximation, they can therefore be treated as Rayleigh scatterers. The radar reflectivity factor for Rayleigh scatterers. Since the target of the observation is often uncertain or not easily categorized, the equivalent reflectivity factor Z_e is introduced. For definition of the equivalent reflectivity factor, the dielectric constant of water drops is

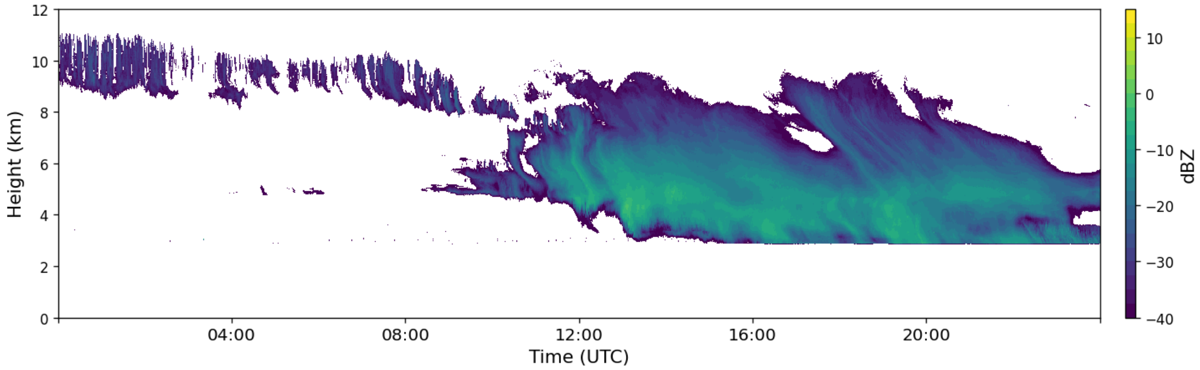

Figure 11, Time-height cross-section of the radar reflectivity factor in dBz observed at Schneefernerhaus on 17 March 2022, 0000–2400UTC. Shown is a dusty cirrus event with a cirrus at 8-12km height between 0000-11000UTC. Taken from Cloudnet..

assumed $||\boldsymbol{K}||$ = 0.93. In the case of liquid water drops with a size smaller than the wavelength of the radar pulse $Z_e = Z$ (Fabry 2015):

(11) $$\boldsymbol{Z_e = \int_0^\infty N(D)D^6 dD.}$$

The radar reflectivity factor Z (see Fig. 11) is defined by the number of particles $N(D)$ of corresponding diameter D per unit Volume. As a result of this relation, the measured reflectivity is proportional to the sixth power of the particle diameter. This makes the radar much more sensitive to the detection of larger particles like ice hydrometeors (Rauber and Nesbitt 2018). Since the values of the radar reflectivity factor often span several orders of magnitude, it is usually expressed in units of decibel:

12) $$\boldsymbol{dBz = 10 \log_{10}(Z)}$$

Another quantity that can be retrieved from radar measurements is the Doppler velocity (see Fig. 12). It can provide information about the vertical velocity of cloud particles. The Doppler velocity can be estimated from the change of phase of the transmitted pulse (Fabry 2015):

(13) $$\boldsymbol{\frac{d\varphi}{dt} = -\frac{4\pi f n}{c} v_{\mathrm{Doppler}}}$$

With f being the frequency of the radar, n the average refractive index of air along the path of the pulse and c the speed of light. However, there can be many different particles with different velocities and positions in the probed volume. Given the Doppler-capabilities of Doppler cloud radars, the distribution of the reflectivity factor of the observed targets is obtained as a function of their motion along the line of sight of the radar. The total return signal, i.e. reflectivity factor, is derived by calculating the integral of the whole Doppler spectrum. The Doppler velocity is finally derived as reflectivity-weighted mean velocity

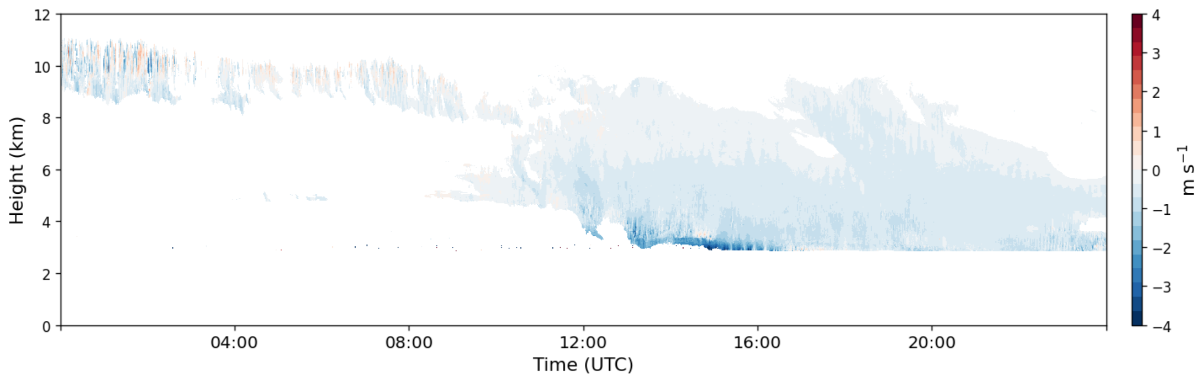

Figure 12, Time-height cross-section of the Doppler velocity in ms-1 observed at Schneefernerhaus on 17 March 2022, 0000–2400UTC. Shown is a dusty cirrus event with a cirrus at 8-12km height between 0000-11000UTC. Taken from Cloudnet.

from all values of the Doppler spectrum detected within the radar time resolution. The structure within a cloud, as well as turbulence or precipitation can be determined from the distribution of Doppler velocities in the cloud.

Cloudnet products and processing chain

Primarily two datasets from the Cloudnet processing chain were used to perform the data analysis for this study. The radar data contains variables from Doppler cloud radar measurements in their original resolution depending on the instrumentation that is available at the corresponding measurement site. For example, the radar data for the measurement site at Schneefernerhaus has a resolution of 8425 sampled profiles per day (~10 seconds resolution) and 488 vertical layers of 30.1 m spatial resolution each. The categorization product contains variables from different measurements (lidar, radar, microwave radiometer) and model data. All the variables in the categorization product are averaged to a common grid to simplify intercomparison between different sites. The Cloudnet grid features a temporal resolution of 30s and a vertical resolution depending on the cloud radar resolution at the measurement site (typically 488 layers). Radar measurement data is corrected for gaseous and liquid attenuation using temperature, pressure and humidity from model outputs and microwave radiometer measurements. The measurement and model data are used to derive a binary categorization mask, which allocates different attributes to each pixel. For example, to identify aerosols, insects and different types of hydrometeors, a target categorization is performed for each pixel (see Fig. 13) (Hogan and O'Connor 2004).

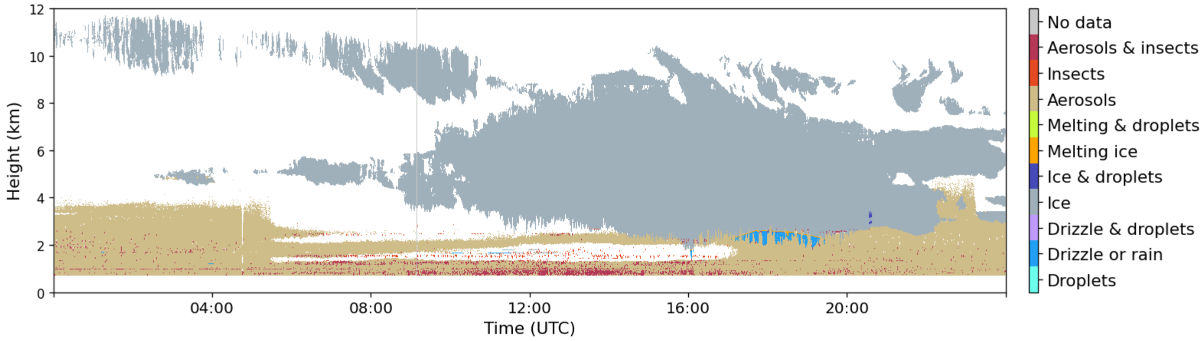

Figure 13, Time-height cross-section of the Cloudnet target classification observed at Schneefernerhaus on 17 March 2022. Taken from Cloudnet.

4.2 Model data

To produce the Cloudnet categorize product, variables like specific humidity, temperature, zonal and meridional wind and pressure from the output of the European Center for Medium Range Weather Forecasts – Integrated Forecast System (ECMWF – IFS) are used. These variables are necessary to ensure continuous data quality and account for effects of atmospheric parameters on the Cloudnet classification algorithm (Hogan and O'Connor 2004). ECMWF – IFS will also be used in this report to analyze possible effects of wind shear and moisture availability on cirrus formation, and to compare model cloud cover to observations. Furthermore, model data from the Copernicus Atmosphere Monitoring Service (CAMS) EAC4 Global Reanalysis, which is a reanalysis of ECMWF – IFS forecast data has been to locate and identify dust layers, as lidar and radar measurements cannot identify dust particles in the presence of clouds.

4.2.1 European Centre for Medium Range Weather Forecasts – Integrated Forecast System (IFS)

The operational forecast model of the ECMWF consists of several coupled model components. The model base is an atmospheric model with a 9 km horizontal resolution and 137 vertical layers for the medium range forecasts (15 days). The model has a reduced Gaussian octahedral grid with 1280 latitude lines. Fig. 14 illustrates the distribution of vertical model layers which follow the model orography at surface level and gradually become smoother with increasing height. For the first 6 days of the forecast the model is rerun with new observational input at 00UTC, 06UTC, 12UTC and 18UTC, for days 7-15 reruns are only performed at 00UTC and 12UTC.

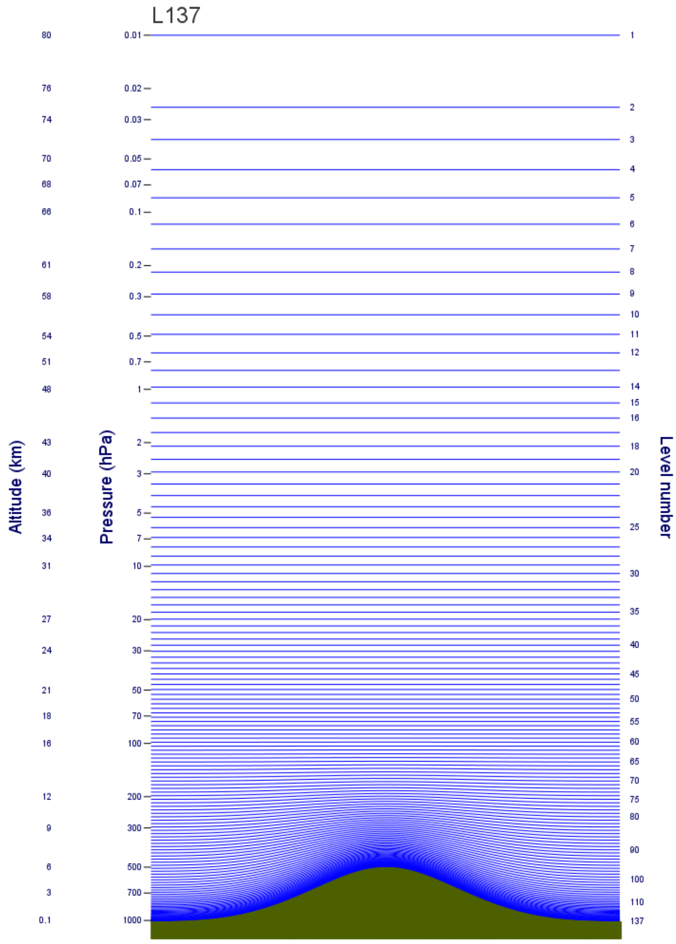

Figure 14, Vertical resolution of ECMWF – IFS L137. Taken from the Copernicus Knowledge Base at https://confluence.ecmwf.int/pages/viewpage.action?pageId=55116796 (access: 24.06.2025).

The atmospheric model is coupled to the following components: ocean wave model (ECWAM – European Centre Wave Model), ocean (NEMO – Nucleus for European Modelling of the Ocean) and sea ice (LIM2 – Louvain-la-Neuve Sea Ice Model version 2) model, land surface model (HTESSEL – Hydrology Tiled ECMWF Scheme for Surface Exchanges over Land) including lake model (Flake – Freshwater Lake model) and a data analysis system (4D-VAR – 4-Dimensional Variational Data Assimilation) which assimilates observational data into the forecast model. The data analysis system performs continuous assimilation to avoid abrupt changes in the model.

The monthly mean aerosol climatology represented in the model is based on CAMS (Copernicus) reanalysis data. While sources and transport of different aerosol classes as well as their radiative effects are included in the operational model, the influence of aerosols on cloud microphysics is not yet considered. A more detailed description of the operational model can be found in the ECMWF Forecast User Guide by Owens and Hewson (2018).

4.2.2 Copernicus Atmosphere Monitoring Service (CAMS) EAC4 Global Reanalysis

The Copernicus Atmosphere Monitoring Service (CAMS) is a service provided by the Earth observation program of the European Union. ECMWF – IFS model output is combined with satellite and in-situ observations to create a global dataset of atmospheric parameters like air pollution, radiation, greenhouse gases and climate forcing.

The ECMWF Atmospheric Composition 4 (EAC4) Global Reanalysis product is a global dataset so far available for the years 2003 to 2024, which will be used in this report to determine position and concentration of dust aerosol in the atmosphere and to evaluate the influence of dust on cirrus formation and structure. CAMS (EAC4) model data is freely accessible in the Atmosphere Data Store (ADS).

The reanalysis data is provided on a reduced Gaussian grid (T255) with 80 km horizontal resolution and 60 vertical layers following the same principles as described for ECMWF – IFS but with a coarser resolution. The geometric height of each model level can be derived from the pressure at model levels, therefore the ECMWF defines a and b coefficients, which describe the pressure component independent of surface pressure (a) and the terrain-following component (b). Different parameters like aerosol composition, atmospheric chemistry, anthropogenic emissions, and biomass burning emissions are provided on 3-hourly analysis fields. (Inness et al. 2019)

Aerosol emission and transport is simulated using the Integrated Forecasting System – Aerosol (IFS – AER) module. Seven different types of aerosols are defined: desert dust, sea salt, black carbon, organic matter, sulphate and ammonium. Desert dust aerosol is split into three separate size bins of 0.03-0.55 µm, 0.55-0.9 µm and 0.9-20 µm diameter. For the emission of dust aerosol, the following parameters are considered: surface winds measured at 10m, soil moisture, surface albedo in the UV to visible range and the fraction of land not covered by vegetation, snow or ice. A lifting threshold wind speed is defined depending on surface parameters like soil roughness and moisture as well as dust characteristics like mineralogy and particle size. It ranges from about 0.1-1 m/s in some boreal areas to up to 5-6 m/s in the Saharan desert. Atmospheric aerosol removal occurs through wet deposition and dry deposition, the latter mainly governed by gravitational settling (e.g. sedimentation). (Rémy et al. 2019)

4.3 Dust load and concentration retrieval (CAMS)

In this section, the process to retrieve dust load and concentration from the CAMS EAC4 Global reanalysis data will be explained. The data provided by CAMS is available as single- and multi-level variables. Single-level variables are only available at surface level (level 60), while multi-level variables are available for all 60 model levels. Multi-level variables that have been used for this report range from model level 60 (surface) to model level 22 (~19-20km above sea level), since processes above that range are most likely do not interfere with the dusty cirrus phenomenon. The following variables have been used for the computation of dust load and dust concentration profiles:

Single-level: Surface pressure, surface geopotential, 2-meter temperature.

Multi-level: Dust Aerosol Mixing Ratios (0.03-0.55 µm; 0.55-0.9 µm; 0.9-20 µm) in kg/kg, model level, specific humidity, temperature, a- and b-coefficients.

4.3.1 Height Calculation from pressure levels

As all CAMS data is provided on model level or pressure level coordinates, the geometric height must be computed to make it comparable to observational data. The height calculation performed for this report follows the guidelines of the ECMWF (Owens and Hewson 2018).

The first step for computing height at a corresponding model level is to compute the pressure at half and full model levels. The pressure at half model levels is computed by adding the *a* and *b* coefficients and multiplying the result with the surface pressure p_{sfc} (14).

(14) $\boldsymbol{p_{half} = a + b * p_{sfc}}$.

The pressure on full model levels is then defined as the mean value between the level above and below the half level pressure values.

The hypsometric equation has been applied to calculate the difference in geopotential between two pressure levels *d* by multiplying the gas constant of dry air R_d with the virtual temperature T_v and the logarithm of the ratio of the pressure of between two subsequent levels p_2 and p_1:

(15) $\boldsymbol{d = R_d * T_v * ln(p_2/p_1)}$

For this step the virtual temperature T_v is calculated from temperature T at model level, the ratio of the gas constants of dry air and water vapor, and specific humidity at model level q.

(16) $\boldsymbol{T_v = T * (1 + 0.607\, q)}$

The surface geopotential provided as single-level variable and the difference in geopotential between half layers were used to integrate upwards and calculate the geopotential on each half model level. Integration from half to full levels was performed to obtain the geopotential at model level. Finally, the geometric height h_G was calculated with the mean radius of the Earth R_E = 6371 km , the geopotential G and the gravitational acceleration g:

(17) $\boldsymbol{h_G = (R_E * \frac{G}{g})/(R_E - \frac{G}{g})}$

4.3.2 Dust load and concentration calculation

Dust aerosol in CAMS is provided as dust mixing ratio in kg/kg and split into three different size bins in the range from 00.3 to 20 µm (see sect. 4.2.2) on a 3-hourly temporal resolution from 22:30 UTC the previous day to 22:30 UTC at the current day. As all variables are only available till 22:30 UTC, the missing values were retrieved from the dataset for the following day.

While super-micron dust particles are very efficient INP and can nucleate ice at temperatures as high as – 10 °C and saturation ratios (w.r.t. ice) of just above 1, sub-micron dust is also an effective INP and can nucleate ice at – 20 °C and saturation ratios of ~ 1.2 (Ansmann et al. 2025; Hoose and Möhler 2012). For this reason, the three size bins were added to retrieve the total dust mixing ratio.

The total dust mixing ratio was multiplied with 1000 to convert kg to g and subsequently divided by the density of air at the corresponding level to obtain the dust concentration in g/m^3 (as displayed in Fig. 15). The density of air ρ was calculated from pressure at model level p, gas constant of dry air R_d and virtual Temperature T_v (18).

(18) $\boldsymbol{\rho = \frac{p}{R_d} * T_v}$

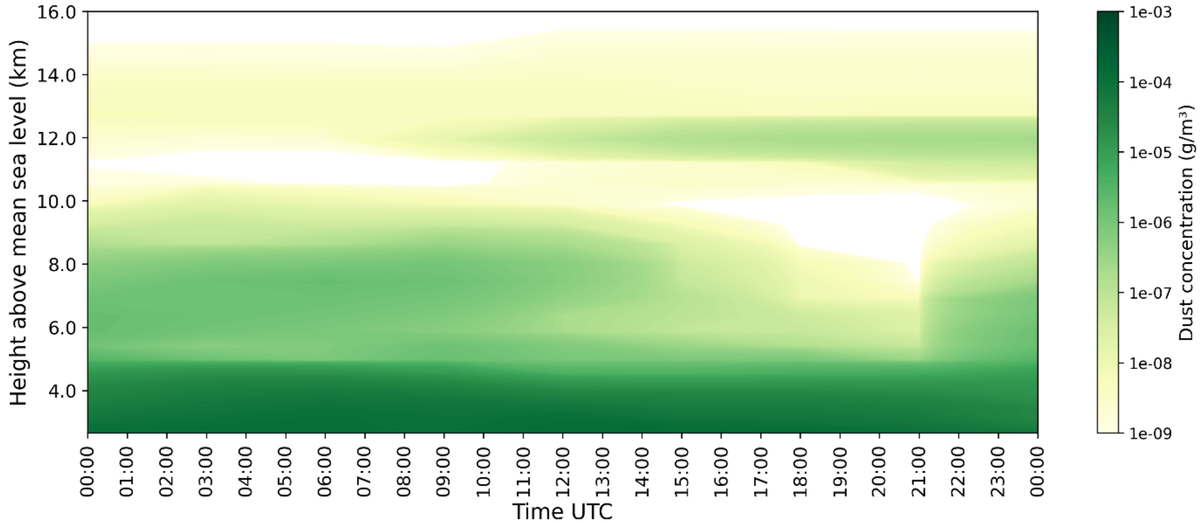

Figure 15, Time-height cross-section of the total dust concentration at Schneefernerhaus on 17 March 2022. Taken from CAMS.

As the dust concentration varies greatly with height and time, a logarithmic scale was chosen for better visualization. In figure 16 an example of the retrieved dust concentrations for the dusty cirrus case on 17th March 2022 is illustrated.

To retrieve a variable which can be easily compared in a yearly statistic, a column dust load in g/m^2 was calculated. The column dust load was integrated upwards over all model levels where the temperature reached a threshold of – 38 °C (235K) to assure that only dust loads at cirrus level are considered.

4.4 Eddy Dissipation Rate

The turbulent structure that can be observed in dusty cirrus cloud decks has been discussed by different studies (Griesche 2016; Kollath 2010; Seifert et al. 2023). An approach to quantify turbulence in the atmosphere is the Eddy Dissipation Rate (EDR). The EDR represents the rate at which large scale atmospheric circulation is dissolved into thermal energy through small scale turbulence. Griesche et al. (2020) have developed an EDR retrieval technique using vertical-pointing Doppler-velocity power spectra, which can be integrated into the Cloudnet processing chain using CloudnetPy. CloudnetPy is a Python package described in Tukiainen et al. (2020) that facilitates the processing of cloud and aerosol remote-sensing data using the Cloudnet processing scheme, as described in detail by **Illingworth et al. (2007)**. This approach to derive the EDR has been used in this study to compare the magnitude of turbulence within cirrus clouds in high dust and low dust conditions.

Eddy Dissipation Rate retrieval

Griesche et al. (2020) applied an EDR retrieval technique originally proposed by Borque et al. (2016), which assumes that turbulence is locally homogeneous and isotropic. In this case, the one-dimensional turbulent energy spectrum *S(k)* can be defined as:

(19) $$\boldsymbol{S(k) = a\varepsilon^{\frac{2}{3}} * k^{-\frac{5}{3}}.}$$

Where $a = 0.5$ is the Kolmogorov constant, ε is the turbulent kinetic energy dissipation rate, and k *is* the wavenumber. Assuming a linear horizontal wind field, the wavenumber can be related to frequency via $k = f / V_h$, where f is the observed frequency and V_h is the horizontal wind speed, and to the length scale L by $k = 2\pi / L$.

This formulation is valid within the inertial subrange — the range of scales or frequencies where energy cascades from larger to smaller eddies without external input or thermal loss. If within this range, the turbulent kinetic energy spectrum follows a -5/3 slope on a log-log scale (energy vs frequency), ε can be determined with Eq. (20) with k_0 the intercept of the linear fit.

(20) $$\boldsymbol{\varepsilon = \left(\frac{10^{k_0}}{a}\right)^{\frac{3}{2}}}$$

For the EDR calculations, continuous Doppler velocity time series of 5 minutes were used. Within these 5 minutes 10% of missing data was allowed and the respective data gaps were interpolated. As accurately isolating the inertial subrange is essential for reliable EDR retrievals using this technique, the inertial subrange was determined by calculating a linear least squares regression of the power spectrum for 17 different wavenumber intervals. EDR was calculated for cases where the slope of the power spectrum follows a − 5/3 slope + − 20 % following Borque et al. 2016.

EDR values for this report were calculated from model and measurement data of the Cloudnet station at Schneefernerhaus for a full year (2022) to obtain EDR values for cirrus cloud cases with and without the presence of mineral dust. Radar observations at Schneefernerhaus are available at a temporal resolution of approximately 10 seconds across 488 vertical levels. To optimize computational efficiency, an EDR value was calculated every 20 seconds at each level based on the 10 second radar data, maintaining a balance between processing time and resolution. To calculate EDR exclusively at cirrus level, the

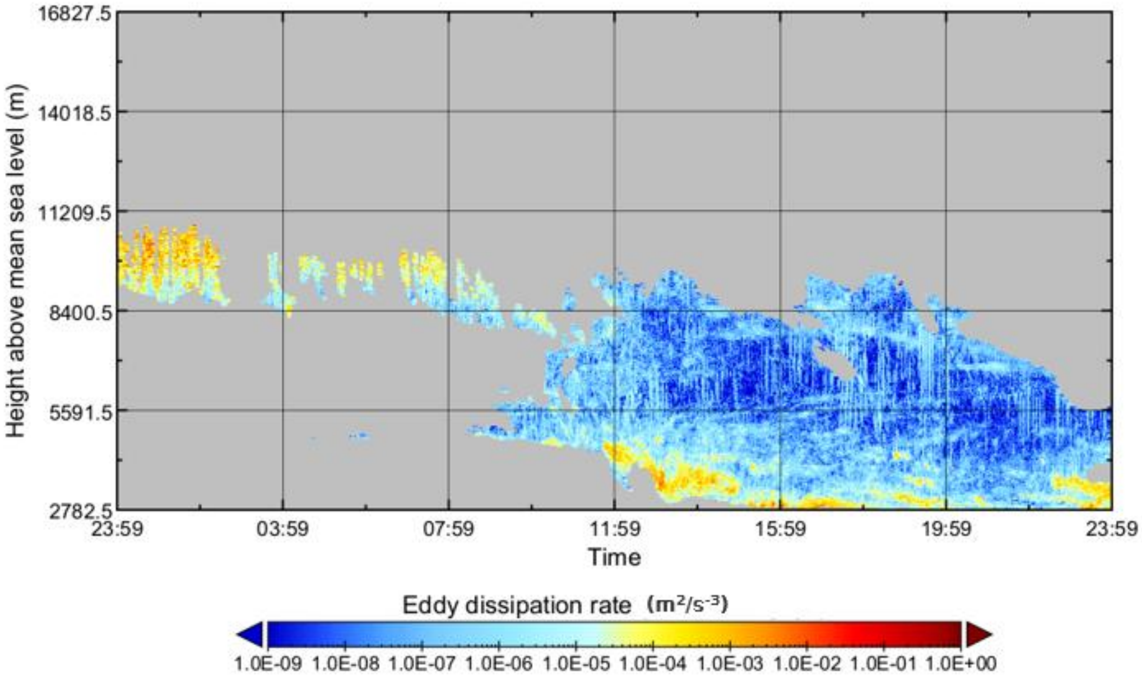

Figure 16, Time-height cross-section of the eddy dissipation rates in detected clouds at Schneefernerhaus on 17 March 2022. Calculated from Cloudnet data.

Cloudnet model temperature was linearly interpolated from the standard Cloudnet grid to the increased EDR resolution. An example of an EDR profile for the dusty cirrus case on 17th March 2022 is illustrated in Figure 16.

4.5 Meteorological parameters from Cloudnet model (ECMWF – IFS)

3.5.1 Cloudnet height correction

The orography in ECMWF – IFS is derived from a global surface elevation dataset with a resolution of 1km. The dataset is then smoothed to a 5km resolution from which a mean orography at model grid points (in the center of each 9x9 km grid box) is calculated. While this procedure in general produced a decent agreement with the observed orography, the smoothing can lead to substantial differences between actual and model orography in mountain areas (Owens and Hewson 2018).

All calculations in this study have been performed on the base of model and observational data from the Cloudnet station at Schneefernerhaus (Zugspitze). In the evaluation of model versus observational data a large difference between the two datasets could be observed. While the real station altitude is at 2653 m above sea level, smoothing of the orography in ECMWF – IFS leads to a model station altitude of 1420 m, a height difference of 1233 m.

The difference in station altitude led to a significant height shift of all model variables, including wind speed and direction, pressure, temperature and specific humidity.

To wait for or produce a reprocessed dataset was outside the scope of this study. Hence, a simple height correction was applied to the categorization file to account for the smoothing error. Applying this approach is unlikely to have introduced significant errors to the results as no products which are calculated using the modelled vertical temperature profile were used. However, this would not work for other Cloudnet products like ice water content, liquid water path or target classification. All of these products are already provided in the categorize file and were computed before the height correction was applied.

In Fig. 17 an intercomparison of temperature and relative humidity profiles from radiosonde measurements at Munich with model profiles of temperature and relative humidity at Munich and Schneefernerhaus on 17th of March 00:00UTC is presented. The left panel of the plot ((a) and (b)) shows profiles before the height correction was applied, the right panel ((c) and (d)) shows the profiles after the correction. The distance between Munich and Schneefernerhaus is roughly 100 km and therefore some discrepancy in the profiles are to be expected. Yet, the height corrected model profiles at Schneefernerhaus are in very good agreement with the radiosonde measurements at Munich.

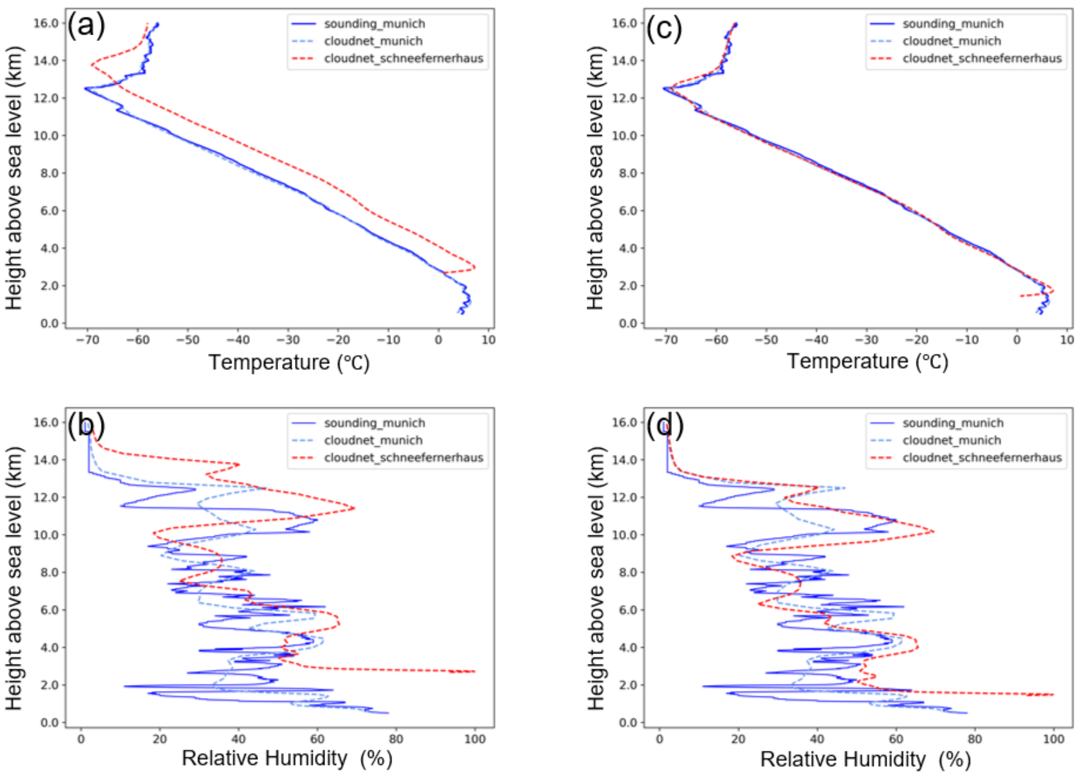

Figure 17, Comparison of temperature and relative humidity profiles at 00:00UTC from Cloudnet model data at Schneefernerhaus and Munich as well as radiosonde measurements at Munich on 17.03.2022 before (a, b) and after (c, d) height correction.

4.5.2 Relative humidity with respect to ice

The availability of moisture seems to be a controlling factor in the formation of dusty cirrus (Griesche 2016; Weger et al. 2018). Cloudnet provides model data of specific humidity, pressure and temperature on the native ECMWF – IFS resolution with 137 vertical layers. To determine the influence of relative humidity on dusty cirrus formation and evaluate model outputs, relative humidity was calculated from the height-corrected Cloudnet model data. For the conversion of specific humidity to relative humidity (w.r.t. ice), several calculations had to be performed. The vapor pressure e was calculated by solving the equation for specific humidity for e with p (pressure), q (specific humidity) and 0.622 the ratio of the gas constants of dry air and water vapor (Eq. 20):

(20) $\boldsymbol{e} = \frac{q*p}{0.622+0378*q}$

Subsequently, saturation vapor pressure over water e_s (Eq. 22) and ice e_{si} (Eq. 23) were calculated using the Magnus equations, based on the model temperature T.

(21) $\boldsymbol{e_s} = \mathbf{6.112} * \boldsymbol{exp}\left(\frac{17.67*T}{T+243.5}\right),$

(22) $\boldsymbol{e_{si}} = \mathbf{6.112} * \boldsymbol{exp}\left(\frac{22.46*T}{T+272.62}\right).$

Relative humidity RH_{ice} could then be calculated for all layers and time steps from the ratio of vapor pressure to saturation vapor pressure:

(23) $\boldsymbol{RH_{ice}} = \left(\frac{e}{e_{si}}\right) * \mathbf{100}.$

Fig. 18 illustrates a time-height cross-section of the relative humidity (blue and red color scale), and radar reflectivity (gray color scale) and wind speed and direction (black arrows) at Schneefernerhaus on 17th March 2022. The dashed blue line indicates the −38 °C Isotherm.

4.5.3 Wind speed and direction

Different theories exist on the origin of the observed turbulent structure of dusty cirrus cloud decks. Seifert et al. (2023) propose that turbulent mixing leads to dust particles being transported into a dust free moist layer forming an initial cirrus cloud which then leads to more turbulence through longwave radiative cooling. Kollath (2010) attributes the turbulent structure of dusty cirrus clouds to nighttime radiative cooling effects. Griesche (2016)

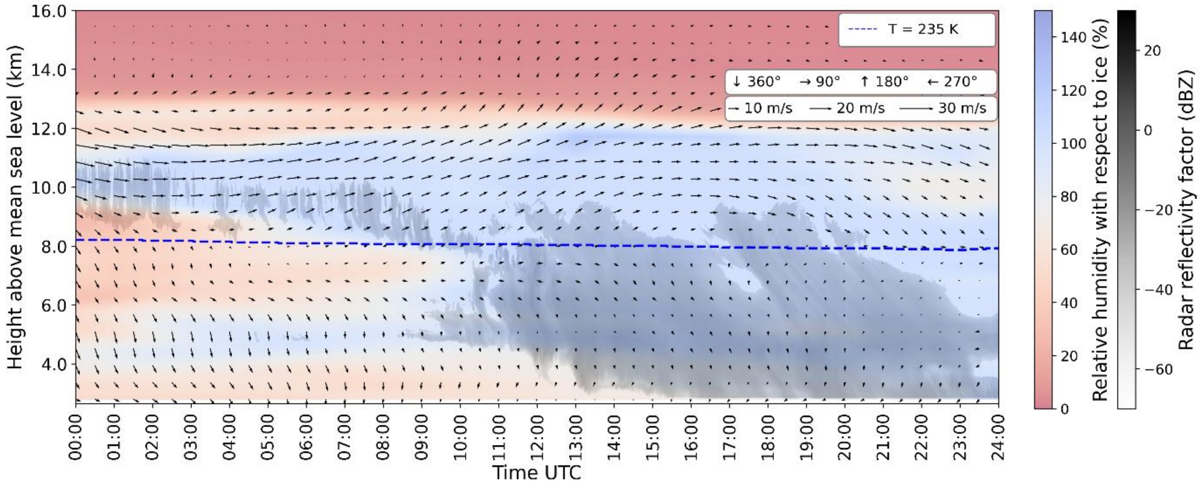

Figure 18, Time-height cross-section of wind speed and direction (black arrows), relative humidity (w.r.t. ice, red and blue colors) and radar reflectivity factor (grey color scale) at Schneefernerhaus from 00:00 to 24:00UTC on 17.03.2022. Computed from Cloudnet data.

highlighted a possible influence of turbulence in dusty cirrus on the forecast skill of NWP in his master's thesis. However, it remains unclear whether the observed turbulence is caused by the presence of dust, or if the turbulence arises from another mechanism and subsequently contributes to the formation of the dusty cirrus clouds. Wind speed and direction have been derived from Cloudnet model data of zonal and meridional wind components to explore the possible influence of wind shear on dusty cirrus turbulence (see Fig. 18).

For calculations of wind speed and direction, the guidelines provided by the ECMWF were followed. Wind speed V was calculated from the zonal u and meridional v wind components by:

(24) $\boldsymbol{V = sqrt(u^2 + v^2).}$

The wind direction ϕ (defined as the direction from which the wind is originating, following meteorological conventions) was calculated using the atan2 function to properly handle all four directional quadrants:

(25) $\boldsymbol{\phi = \left(atan2(-u, -v) * \frac{180}{\pi}\right) mod\ 360.}$

4.6 Statistical Analysis of high-dust and low-dust-cirrus clouds

For the statistical analysis of the relationship between the occurrence of mineral dust and cirrus turbulence, a timeline was created illustrating column dust load (orange), normalized cloudpixel count (blue) and EDR value (vertical color bars: light green ≤ 15th percentile;

dark green 15th to 85th percentile; brown ≥ 85th percentile) for the whole of 2022 at Schneefernerhaus. Dust load is calculated as column value for heights at cirrus level only, as described in section 3.3.2. The dust load represented in Fig 19 is the daily mean value of dust loads at all timesteps. The cloudpixel count was calculated as the total number of EDR values encountered at cirrus height (above the first height where T ≤ −38 °C), EDR was calculated for all cloudpixel detected by the radar signal. All cloudpixel counts were then normalized to 1 by the largest daily cloudpixel count during the whole year. EDR values are also given as a daily mean value and split into three different categories: unusually low values were defined as below the 15th percentile while unusually high values were defined as above the 85th percentile, medium values represent the range in between.

The Cloudnet station at Schneefernerhaus was chosen because it meets several requirements. First it provides a sufficiently high vertical and temporal resolution. Second, the data coverage at Schneefernerhaus is comparably high, as many Saharan dust events do not reach much further north. While other stations (e.g. Jülich or Leipzig) provide a slightly better temporal resolution and have longer time series of continuous measurements, they do not observe as many Saharan dust events. Therefore, Schneefernerhaus presents a good compromise, even though some effect of local topography on the atmospheric structure is to be expected.

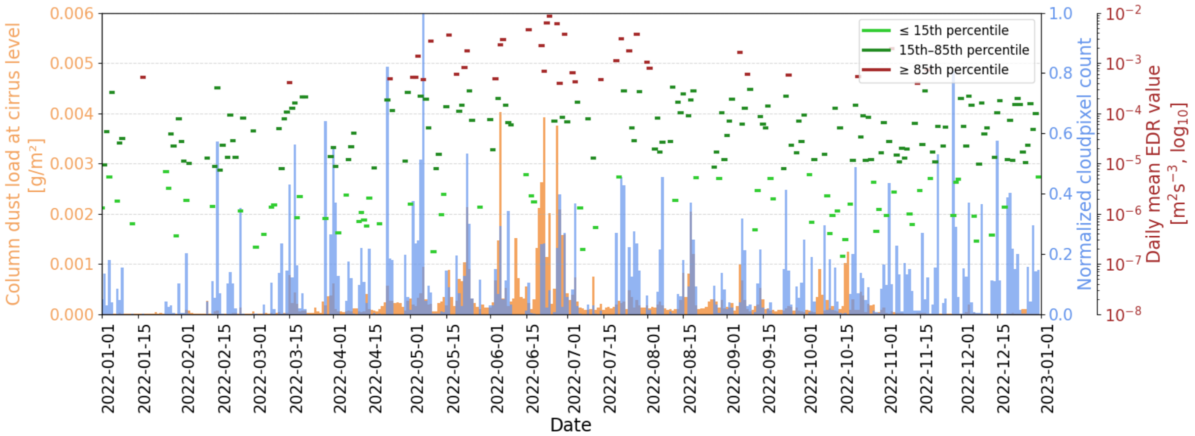

Figure 19, Timeline of dust load, cloudpixel count and EDR value at Schneefernerhaus for 2022. Computed from CAMS model and Cloudnet model and measurement data.

5 Results

In this Section the relationship of cirrus cloud turbulence and atmospheric dust load, based on observational and modeled data from the Schneefernerhaus station in 2022 will be investigated. The focus lies on the variation of eddy dissipation rate (EDR) under different dust conditions, highlighting key differences in turbulence between dusty and non-dusty cirrus events. First, the EDR distributions for high and low dust days are directly compared (sect. 5.1), followed by a quantitative assessment of the correlation between dust load and EDR (sect. 5.2). Subsequently, three distinct scenarios are examined using combined observational and model-based data (sect. 5.3). These include the vertical distribution of dust and humidity, wind profiles, and the spatial structure of cirrus clouds. Special attention is placed on processes relevant to cirrus formation and turbulence. These results provide a base for evaluating current theories on dusty cirrus formation and the ability of numerical models to simulate the associated microphysical and dynamical processes.

5.1 Turbulence of dusty cirrus vs normal cirrus

For a direct comparison of cirrus turbulence in high and low dust scenarios, all calculated EDR values at cirrus level for the year 2022 at Schneefernerhaus were sorted by the respective daily mean dust load. In the analyzed period, the 15th percentile dust load was $7.24 \bullet 10^{-6}$ g/m^2, while the 85th percentile was $3.40 \bullet 10^{-4}$ g/m^2. Figure 20 contrasts the distribution of EDR for all days where the dust load was below the 15th percentile (blue) compared to all days where the dust load reached above the 85th percentile (brown). The EDR counts were then normalized to one, to illustrate them by their frequency of occurrence.

The EDR values span a wide range from ~ $1 \bullet 10^{-10}$ to $1 \bullet 10^{-2}$ m^2/s^3 for low dust scenarios and from ~ $1 \bullet 10^{-9}$ to 1 m^2/s^3 for high dust scenarios respectively, and a clear difference is evident in the peaks of the two distribution curves. The peak of each curve was calculated as the highest average bin count across 10 consecutive bins. The highest occurrence of EDR values in low-dust conditions was observed around $5.0 \bullet 10^{-7}$ m^2/s^3, whereas for high-dust conditions the peak is shifted by roughly two orders of magnitude to a value of $1.2 \bullet 10^{-5}$ m^2/s^3. The overlap of the two distributions can be attributed partly to the method how low- and high-dust conditions were separated. EDR values from an entire day are assigned to

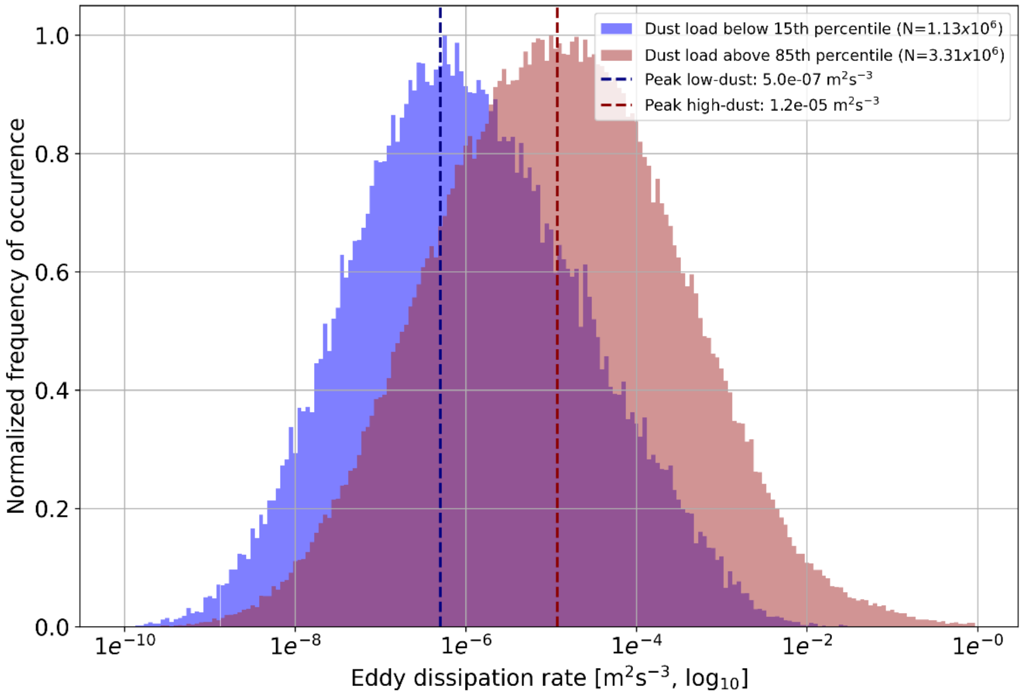

Figure 20, Comparison of the distribution of eddy dissipation rates for high- and low-dust scenarios at Schneefernerhaus for 2022. Computed from CAMS model and Cloudnet model and measurement data.

one of the two distributions based on the daily mean dust load. This approach can lead to misclassification in cases where the dust load is subject to strong changes over the course of the day. A more robust approach would be to retrieve EDR values for explicit time windows with high dust loads only. However, the coarse three-hour resolution of the CAMS dust aerosol products limits the accuracy of this approach. Ground-based lidar observations provide in principle much higher resolved dust observations under cloud free conditions. However, under dusty cirrus conditions, strong signal attenuation prevents reliable lidar-based dust retrievals. In these cases, dust could only be observed between the clouds.

5.2 Correlation between dust load and EDR

The distribution of EDR in high and low dust conditions illustrated in sect. 5.1 shows that high cirrus turbulence is more likely to occur in the presence of high dust loads. However, from the simple distribution presented, it remains unclear if there is a direct correlation between the amount of dust in the atmosphere and the observed turbulence. To explore this possibility, a scatter plot of the daily mean EDR compared to the daily mean dust load calculated for each day of 2022 is shown in Figure 21. For a more detailed view on the

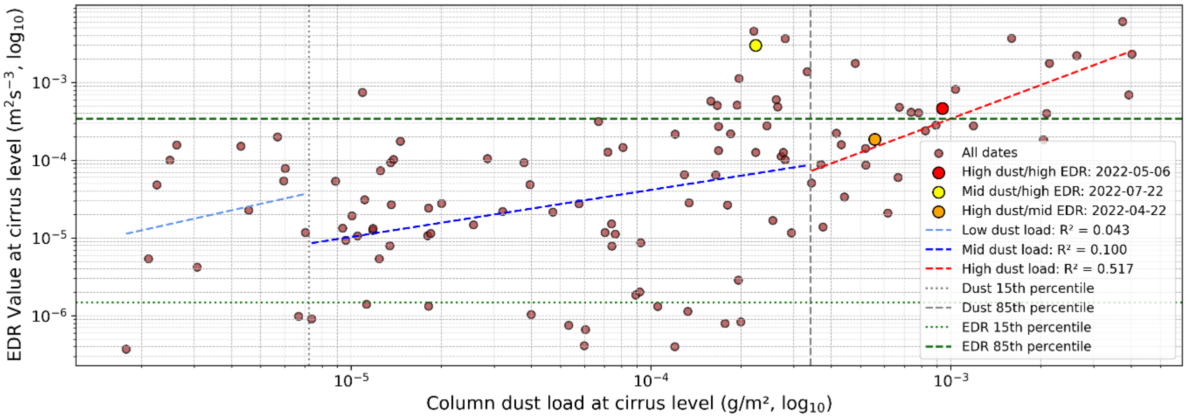

Figure 21, Correlation of EDR value and column dust load at cirrus level with a segmented linear fit for low, mid and high dust conditions at Schneefernerhaus for 2022. Computed from CAMS model and Cloudnet model and measurement data.

correlation between dust load and EDR a segmented linear fit was computed for the three different dust regimes:

- Low dust (≤ 15th percentile, light blue dashed line in Fig. 21)
- Mid dust (15th – 85th percentile, dark blue dashed line in Fig. 21)
- High dust (≥ 85th percentile, red dashed line in Fig. 21)

Since days with very low cloud cover contribute equally to the correlation despite having significantly lower actual information content, a low-cloudpixel correction was introduced. This was done by filtering out all days with a normalized cloudpixel count below 0.1 (10% of the maximum number of observed cloudpixel).

Figure 21 is further divided into 9 subsections ranging from low dust load/low EDR (lower left corner) to high dust load/high EDR (upper right corner). In the first segment (low dust conditions, left part of Fig. 21), low and medium EDR can be observed with a maximum EDR of ~ $2.0 \cdot 10^{-4}$ m^2/s^3. With an R^2 of 0.043, no statistical correlation between dust load and EDR was found in this segment. The second segment (moderate dust conditions, middle part of Fig. 21) shows the widest range of EDR values, with the highest EDR values (around $4 \cdot 10^{-3}$ m^2/s^3) occurring at higher dust loads above $2.0 \cdot 10^{-4}$ m^2/s^3. Although a visible slope is present from lower EDR at lower dust loads to higher EDR at higher dust loads in this segment, there is no statistically relevant correlation (R^2 = 0.100). In the third segment (high-dust conditions, right part of Fig. 21), EDR values only appear in the upper half of the dust load range between ~ $1.0 \cdot 10^{-5}$ m^2/s^3 and $1.0 \cdot 10^{-2}$ m^2/s^3. A clear positive slope and a significant statistical correlation is observed with an R^2 of 0.517.

The daily average dust load and the respective EDR values are summarized for the three different segments of Fig. 21 in Table 1-3. Table 1 shows cases high daily mean dust load (≥ 85th percentile) and high daily mean EDR value (≥ 85th percentile). High daily mean dust load (≥ 85th percentile) and moderate daily mean EDR value (≥ 15th percentile and ≤ 85th percentile) are summarized in Table 2, and moderate daily mean dust load (≥ 15th percentile and ≤ 85th percentile) and high daily mean EDR value (≥ 85th percentile) in Table 3.

Table 1: High daily mean dust load / high daily mean EDR value

Date	Mean EDR [m^2/s^3]	Norm. cloudpixel count	Dust load [g/m^2]
2022-03-15	4.68e-04	0.53	0.0008
2022-05-06	4.24e-04	1.00	0.0012
2022-05-22	8.95e-04	0.13	0.0014
2022-05-23	1.88e-03	0.58	0.0027
2022-06-03	3.59e-04	0.20	0.0007
2022-06-05	2.15e-03	0.32	0.0045
2022-06-21	1.99e-03	0.27	0.0026
2022-06-22	5.70e-04	0.31	0.0043
2022-06-27	5.94e-03	0.23	0.0041
2022-06-28	5.97e-04	0.45	0.0023
2022-06-30	3.56e-03	0.29	0.0016
2022-07-04	4.76e-04	0.47	0.0007
2022-07-25	1.49e-03	0.29	0.0006

Table 2: High daily mean dust load / medium daily mean EDR value

Date	Mean EDR [m^2/s^3]	Norm. cloudpixel count	Dust load [g/m^2]
2022-03-17	1.29e-04	0.62	0.0008
2022-03-31	1.26e-05	0.33	0.0004
2022-04-01	1.85e-05	0.67	0.0007
2022-04-22	1.60e-04	0.87	0.0007
2022-05-05	1.71e-04	0.60	0.0004
2022-05-24	3.16e-04	0.36	0.0012
2022-06-07	1.34e-04	0.17	0.0006
2022-08-15	3.00e-04	0.24	0.0009
2022-08-18	1.63e-04	0.43	0.0024
2022-08-19	2.78e-04	0.25	0.0012
2022-09-07	6.11e-05	0.39	0.0008
2022-09-14	8.58e-05	0.26	0.0006
2022-10-23	3.21e-05	0.16	0.0007
2022-10-24	9.10e-05	0.15	0.0005

Table 3: Medium daily mean dust load / high daily mean EDR value

Date	Mean EDR [m^2/s^3]	Norm. cloudpixel count	Dust load [g/m^2]
2022-04-23	4.86e-04	0.19	0.0003
2022-05-02	5.15e-04	0.44	0.0002
2022-05-03	6.20e-04	0.29	0.0002
2022-05-04	1.22e-03	0.29	0.0004
2022-05-19	5.31e-04	0.25	0.0003
2022-06-16	4.62e-03	0.11	0.0002
2022-07-20	1.04e-03	0.33	0.0003
2022-07-22	2.84e-03	0.48	0.0002
2022-07-28	3.15e-03	0.30	0.0003
2022-09-25	4.16e-04	0.23	0.0002
2022-11-18	5.89e-04	0.18	0.0000

As can be seen in Figure 21, scenarios with low dust load (≤ 15th percentile) and high EDR value (≥ 85th percentile) or high dust load (≥ 85th percentile) and low EDR value (≤ 15th percentile) were not observed. From the observed dates, an exemplary one was chosen for each scenario, which will be analyzed in the following section. The chosen scenarios are marked in the respective table as well as in Fig. 21 (red: high dust/high EDR; yellow: mid dust/high EDR; orange: high dust/mid EDR).

5.3 Case Studies

For the analysis of the exemplary scenarios, a combined plot was created for each case, incorporating all derived parameters from both model and observational data. The radar reflectivity was used to identify the location and extent of the cirrus cloud layer. A dust concentration contour was added to assess the correlation between cirrus and the presence of dust. Wind speed and direction are represented by arrows of varying length and orientation to qualitatively evaluate the potential influence of wind shear (speed and directional) on cirrus formation. Relative humidity (w.r.t. ice) was included as a color contour to investigate the role of humidity in cirrus formation and to test the validity of dusty cirrus formation theories. Finally, an isoline was added at 238 K (-38 °C) to indicate the altitude, above which only cirrus clouds can be observed.

5.3.1 High dust load and high EDR – 6th May 2022

In Figure 22, a typical dusty cirrus cloud, characterized by high daily mean dust load and high daily mean EDR values is presented. The grey shaded area at height above the 235 K isotherm (blue dashed vertical line) reveals the presence of a cirrus cloud almost throughout the whole day. The observed cirrus cloud is spatially coherent with an elevated dust concentration of more than $5.0 \cdot 10^{-7}$ g/m^3. Both features are at the same altitude, suggesting that cirrus formation occurs within the dust layer, rather than above or below it. This stands in contrast to the mixing instability theory (A. Seifert et al. 2023), which presumes that dusty cirrus clouds form at the interface between a dry dust-laden layer and an overlying, dust-free moist air layer. Stable wind directions and significant moisture availability within the air layer of the dusty cirrus further support the in-layer formation hypothesis. A slight reduction of moisture within the observed cirrus cloud at ~9 km (visible by slightly reddish colors at that height) can likely be explained by heterogeneous nucleation processes. When dust particles act as INP, they scavenge water vapor from the surrounding air through heterogeneous nucleation, supersaturation can decrease and suppress homogeneous nucleation as a consequence (Ansmann et al. 2025; Kärcher et al. 2022).

The dust concentration at cirrus level is about $5 \cdot 10^{-7}$ g/m³ or ~ 0.5 µg/m³. Assuming standard atmospheric conditions according to the International Standard atmosphere (ISA), the density of air at cirrus level is around 0.5 kg/m³. This translates to a maximum dust concentration of ~ 1 µg/kg in the presented case. This value is much lower than the dust concentration threshold of 50 µg/kg used in the dusty cirrus parametrization of Seifert et al. (2023).

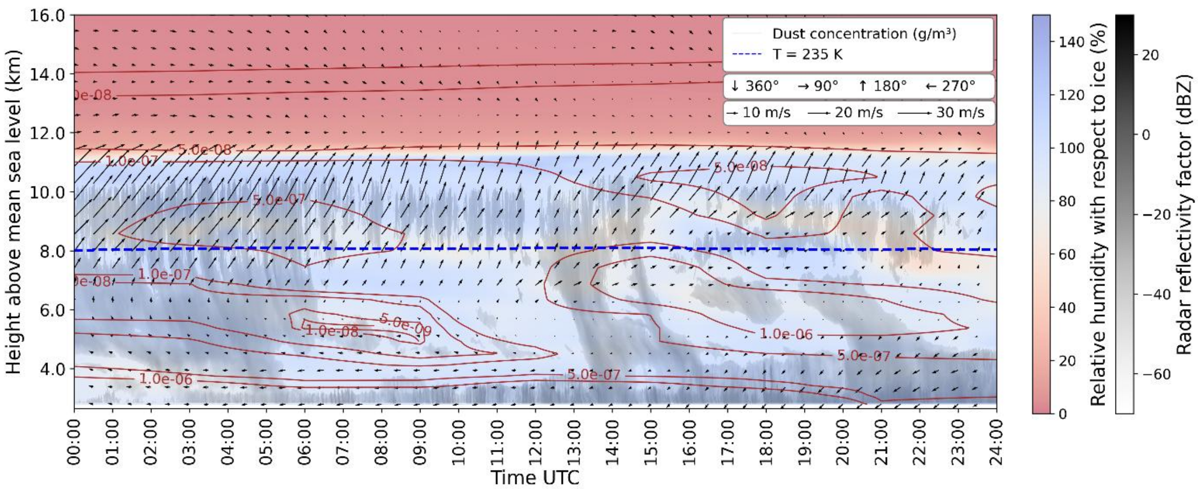

Figure 22, Time-height cross-section of radar reflectivity (grey color scale), relative humidity (w.r.t. ice, red and blue color scale), wind speed and direction (black arrows) , dust concentration (brown contour lines) and −38 °C isotherm (vertical dashed blue line) at Schneefernerhaus on 6 May 2022. Calculated from Cloudnet and CAMS data.

The nighttime radiative cooling theory is primarily based on the convective structure of dusty cirrus clouds, as observed in satellite imagery **(Kollath 2010)**. This convective structure is most apparent in the early morning and appears to dissipate throughout the day. However, satellite images lack vertical resolution, it is therefore possible that the enhanced visibility of the convective structure in the morning is due to shadow effects caused by the lower sun zenith angle. With an increasing sun zenith angle, these shadow effects are reduced, potentially creating the appearance that the convective structure has dissolved.

Figure 23 shows time-height cross-section of calculated EDR values for the dusty cirrus case on 5th May 2022. While the highest occurrence of enhanced EDR values was observed during the night and up to roughly two hours after sunrise (00:00–06:00 UTC at 8500–10,000 m), similarly elevated EDR values were reached during the day, particularly between 10:00 and 12:00 UTC at the same altitude range. The highest observed EDR coincided with peak dust concentrations, raising the question of whether dust presence or radiative cooling plays the dominant role in generating cirrus cloud turbulence in this case. Additionally, the cloud cover is generally decreasing throughout the day, which makes it difficult to reach a clear conclusion. Although wind shear (in direction and speed) is evident at ~ 11500 m altitude, it is well separated from the cirrus cloud top by almost 1000 m, which suggests a rather limited role in driving the observed turbulence.

Figure 24 compares the observed radar reflectivity (upper panel) with the Cloudnet model cloud fraction based on ECMWF – IFS (lower panel). While any detected signal within the

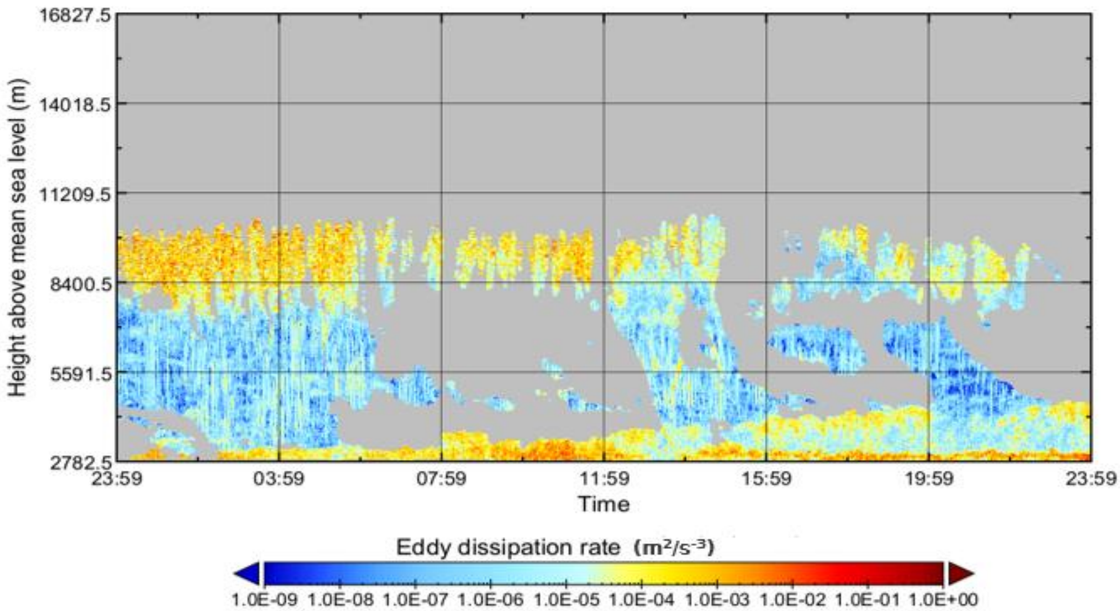

Figure 23, Time-height cross-section of eddy dissipation rates in detected clouds at Schneefernerhaus on 06th May 2022. Calculated from Cloudnet data.

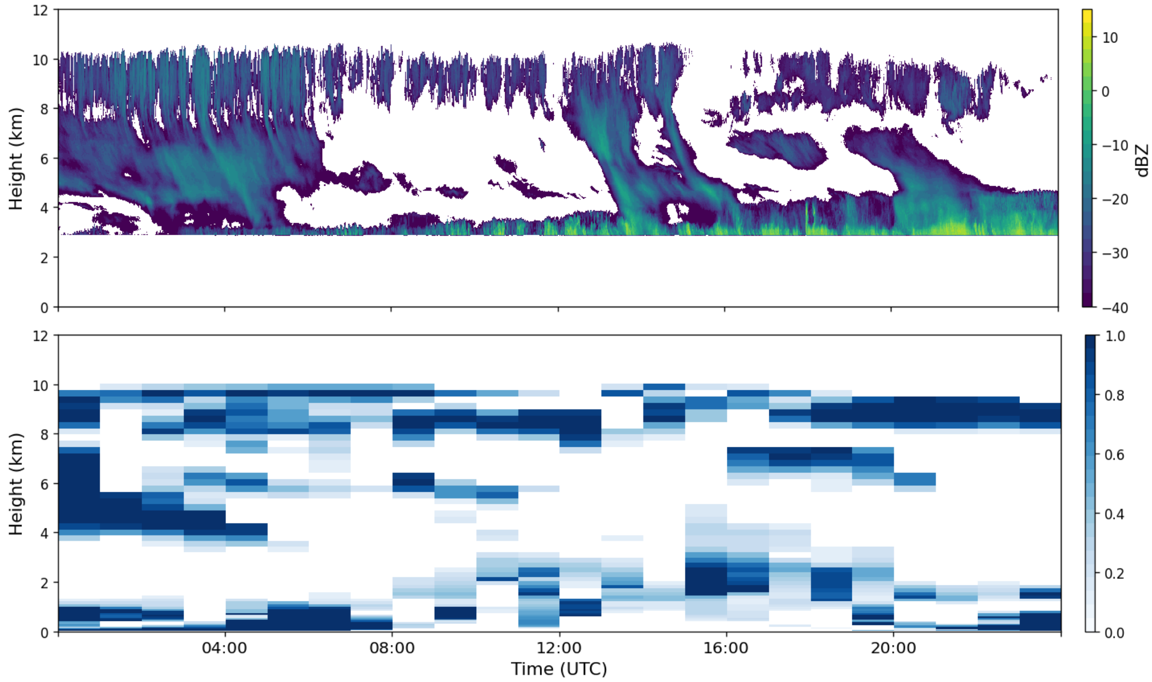

Figure 24, Time-height cross-section of radar reflectivity (upper panel) and model cloud fraction (lower panel) at Schneefernerhaus on 6 May 2022. Taken from Cloudnet.

presented radar reflectivity range can be interpreted as a hydrometeor, a higher signal indicates either a higher number or larger size of the oberved hydrometeros. The cloud fraction is a model product which combines different hydrometeor and precipitation classes. A cloud fraction of 1 indicates a cloud cover of 100 % within the respective pixel.The radar reflectivity reveals a dusty cirrus cloud with a distinct turbulent structure between 8000 and 10000m almost throughout the day. The modeled cloud fraction shows reasonable agreement in terms of the general height and horizontal extent of the cirrus cloud but struggles to capture the turbulent structure in detail. The differences may be attributed to the coarse vertical and horizontal resolution of the model. Additionally, the representation of convective or mixed-phase clouds appears to be limited, particularly in dusty regions (e.g. 12:00 to 16:00 UTC at ~ 3000m to 7500m). This suggests that the model struggles to represent cloud microphysical processes and vertical air movement in high dust conditions, highlighting the need for improved ACI parameterizations.

5.3.2 Moderate dust load and high EDR – 22nd July 2022

The second case depicts a convective cloud system between 16:00 and 24:00 UTC on 22nd July 2022. While a high daily mean EDR value of $2.84 \cdot 10^{-3}$ m^2/s^3 was derived, the daily mean dust load is only moderate (~ $2.0 \cdot 10^{-4}$ g/m^3). However, closer inspection of Fig. 25 reveals elevated dust concentrations of 0.01 to 0.1 μg/m³ at cirrus level, when the cloud was

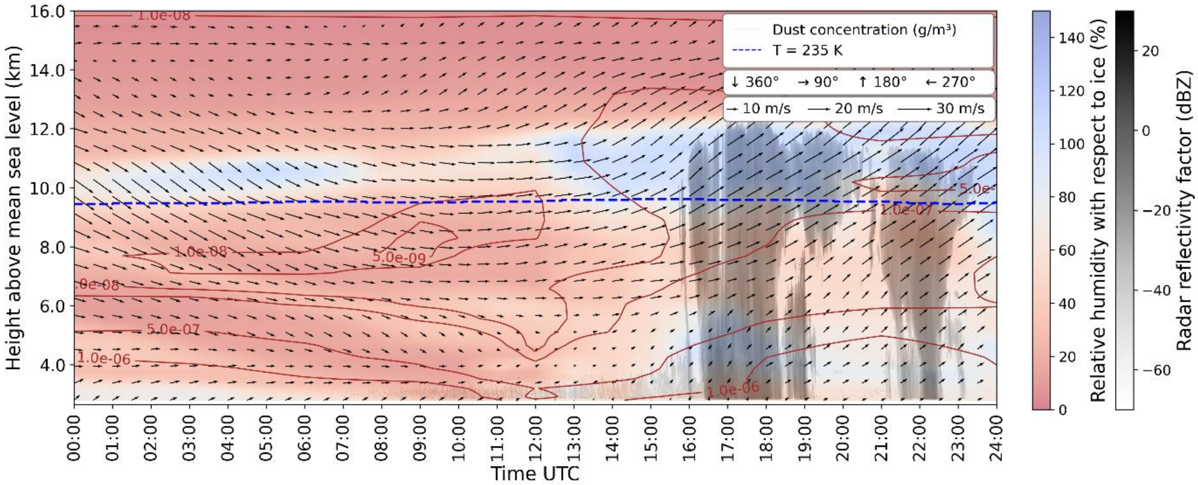

Figure 25, Time-height cross-section of radar reflectivity (grey color scale), relative humidity (w.r.t. ice, red and blue color scale), wind speed and direction (black arrows) , dust concentration (brown contour lines) and −38 °C isotherm (vertical dashed blue line) at Schneefernerhaus on 22 July 2022. Calculated from Cloudnet and CAMS data.

observed (after 16:00 UTC), as well as increased relative humidity. This case does not reach the 85th percentile threshold used to define dusty days, since the dust load is calculated as a daily mean value. A similar pattern can be observed for several cases that were classified as mid dust/high EDR.

Although dusty cirrus typically appears as a distinct cloud layer, in this case it appears to be part of a convective system. Despite differing from the usual dusty cirrus structure, the elevated dust concentration again coincides with a peak in relative humidity and increased turbulence (see Fig. 26), supporting the hypothesis of in-layer formation. The observed

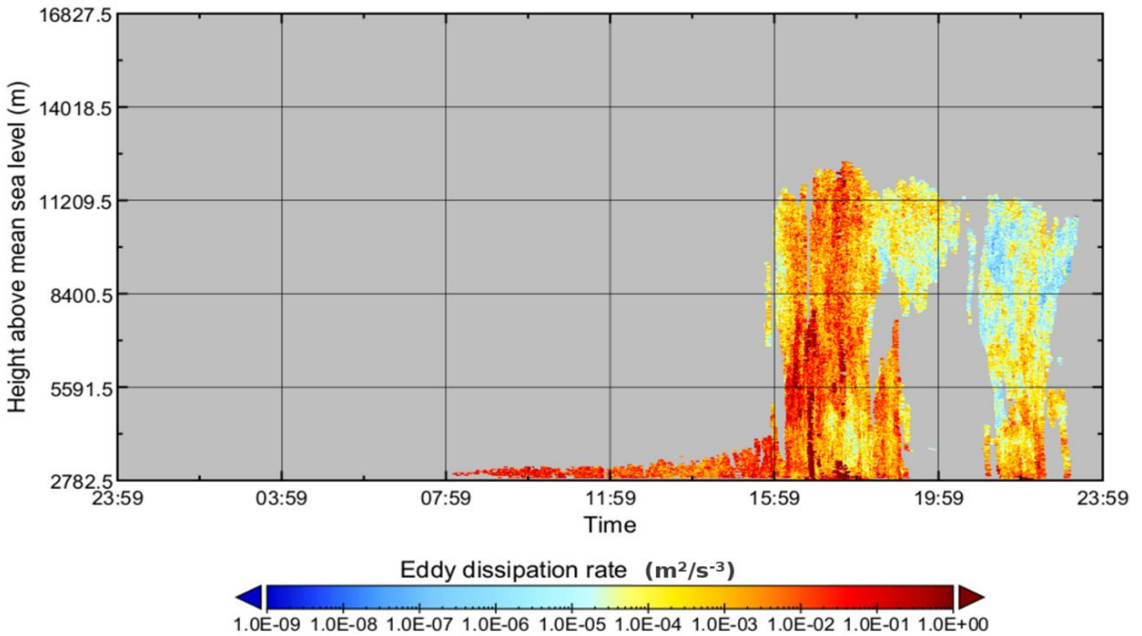

Figure 26, Time-height cross-section of eddy dissipation rates in detected clouds at Schneefernerhaus on 22nd July 2022. Calculated from Cloudnet data.

cloud exhibits a distinct convective structure, suggesting that turbulence and relative humidity at cirrus level might also result from convective lifting rather than microphysical processes. However, it is also possible that, while convective lifting might be responsible for the transport of dust into the upper troposphere, the turbulence at cirrus level might in turn be related to the presence of dust. Finally, no significant wind shear in the region of the cloud was observed in the vertical wind profile, indicating that the observed turbulence is likely not shear-induced.

A comparison of the radar reflectivity and Doppler velocity to the model cloud fraction as shown in Fig. 27, leads to similar conclusions as in the high dust/high EDR case discussed in the previous section. While the general altitude of the cirrus and its horizontal extend are in decent agreement, the model struggles to capture the vertical extend of the cloud, especially in regions with elevated dust concentration or strong vertical air movement (e.g. after 16:00 UTC at ~ 3000 to 8000m).

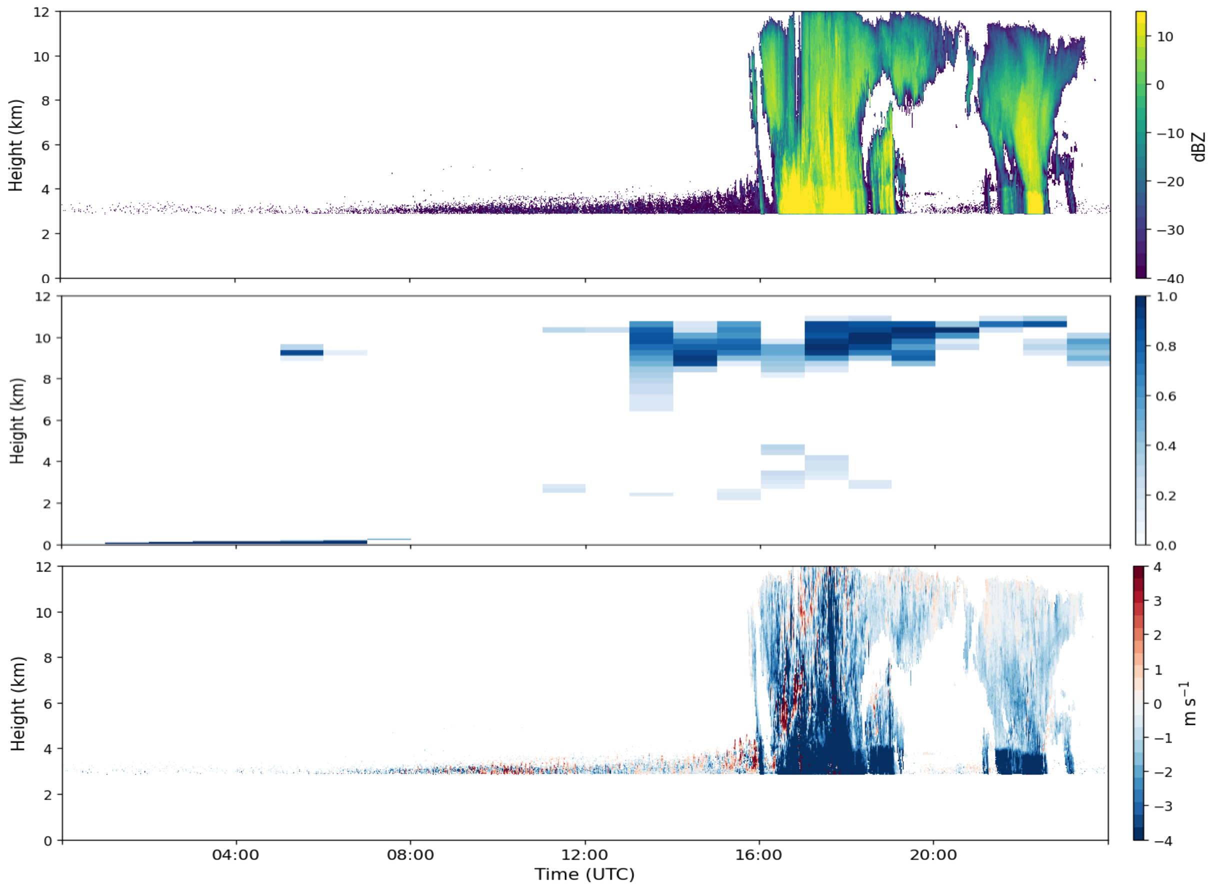

Figure 27, Time-height cross-section of radar reflectivity (upper panel), model cloud fraction (middle panel) and Doppler velocity (lower panel) at Schneefernerhaus on 22 July 2022. Taken from Cloudnet

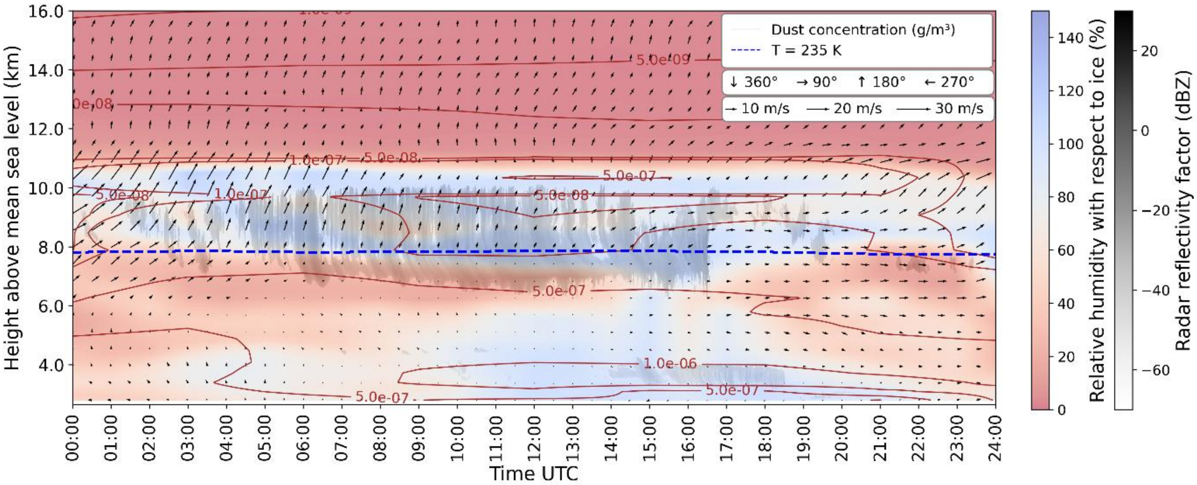

Figure 28 Time-height cross-section of radar reflectivity (grey color scale), relative humidity (w.r.t. ice, red and blue color scale), wind speed and direction (black arrows), dust concentration (brown contour lines) and −38 °C isotherm (vertical dashed blue line) at Schneefernerhaus on 22 April 2022. Calculated from Cloudnet and CAMS data.

5.3.2 High dust load and moderate EDR – 22nd April 2022

In the third case study, depicted in Fig. 28, a scenario with a high daily mean dust load ($\sim 7.0 \cdot 10^{-4}$ g/m^3) but only moderate daily mean EDR values ($1.60 \cdot 10^{-4}$ m^2/s^3) is examined. The dust load in this case just meets the 85th percentile threshold with the highest encountered dust concentrations at cirrus level around 0.5 µg/m³. However, the highest dust concentrations were observed above the cirrus cloud, while lower dust load values between 0.05 and 0.1 µg/m³ were observed within the cirrus cloud layer. This is in contrast to the first dusty cirrus case, where the dust load was strongly concentrated within the cirrus cloud layer. The reason for the comparatively low turbulence in this case cannot completely be explained by the applied methods, suggesting that high dust load alone does not necessarily suffice to produce the high turbulence observed in dusty cirrus clouds. Most similar cases with a daily mean dust load just above the 85th percentile threshold showed above average but below 85th percentile EDR values. Figure 28 reveals a cirrus cloud between 01:00 and 20:00 UTC at an altitude of 8000 to 10000 m. In this case the cirrus cloud extends well below the −38 °C isotherm, unlike the more distinct, elevated cirrus layers seen in other dusty cirrus cases. This vertical extension may affect the turbulence structure of the cloud, possibly contributing to the reduced EDR.

The EDR of the presented dusty cirrus cloud on 22nd April 2022 are shown in Figure 29. In this case, the highest EDR values occurred in the morning between 04:30 and 10:00 UTC — shortly after sunrise at approximately 04:15 UTC — and aligned with peak dust

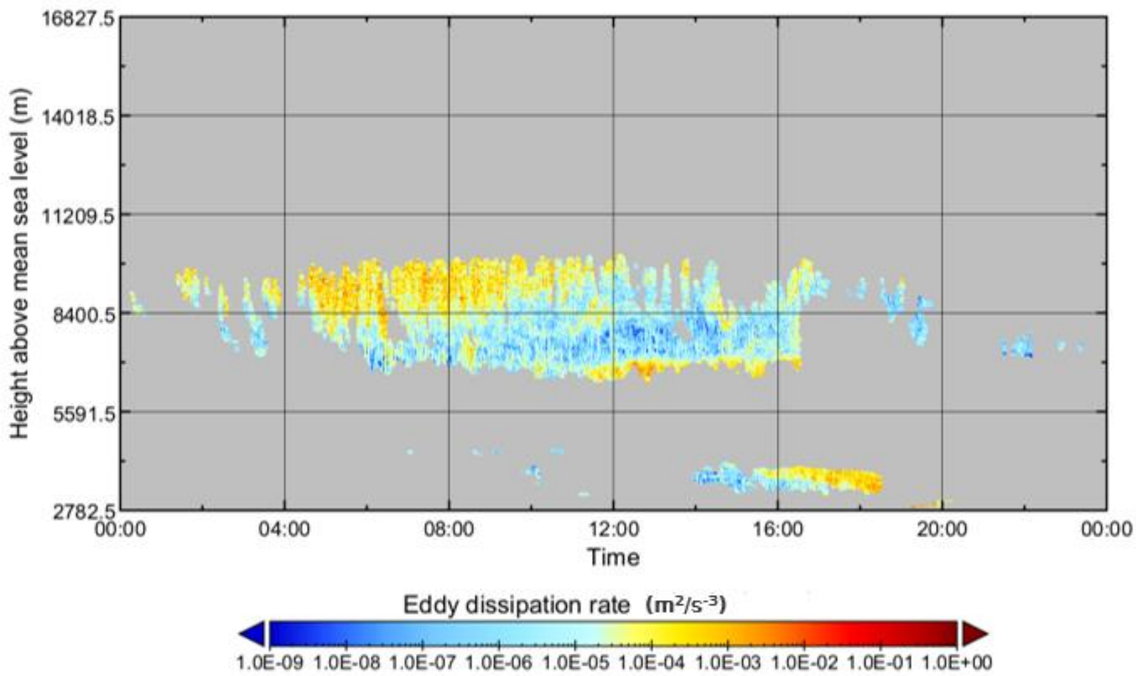

Figure 29, Time-height cross-section of eddy dissipation rates in detected clouds at Schneefernerhaus on 22nd April 2022. Calculated from Cloudnet data.

concentrations. A decrease in EDR can be observed towards the afternoon, again coinciding with a general decrease in cloud cover and dust concentration. While there seems to be a decrease of EDR in both of the observed dusty cirrus cases, more data is necessary to develop a statistical correlation and evaluate the nighttime radiative cooling theory. The effect of wind shear on the observed cirrus turbulence again seems to be negligible.

Figure 30 shows a comparison between radar reflectivity and model cloud fraction as described in Fig. 24. The dusty cirrus is rather poorly represented in the model data in this particular case. While the altitude of the simulated cloud roughly matches the observations, vertical extent and cloud thickness are not accurately depicted. Additionally, there are noticeable gaps especially between 10:00 and 11:00 UTC as well as 13:00 to 15:00 UTC in the modelled cloud compared to the observations. These discrepancies raise questions about the model's capability of resolving microphysical processes and small-scale turbulence.

Following the approach of Ansmann et al. (2025), Fig. 31 presents an analysis of how much lofting an air parcel at cirrus level would require to reach the supersaturation threshold necessary for heterogeneous ice nucleation — specifically for the modelled cirrus gap observed between 14:00 and 15:00 UTC. The figure consists of two plots with time in s on the x-axis. In the upper panel, the y-axis displays height and temperature, and the line represents the ascent of an air parcel moving at a mean updraft velocity of 0.349 m/s, corresponding to the mean Doppler velocity derived from radar measurements at cirrus level

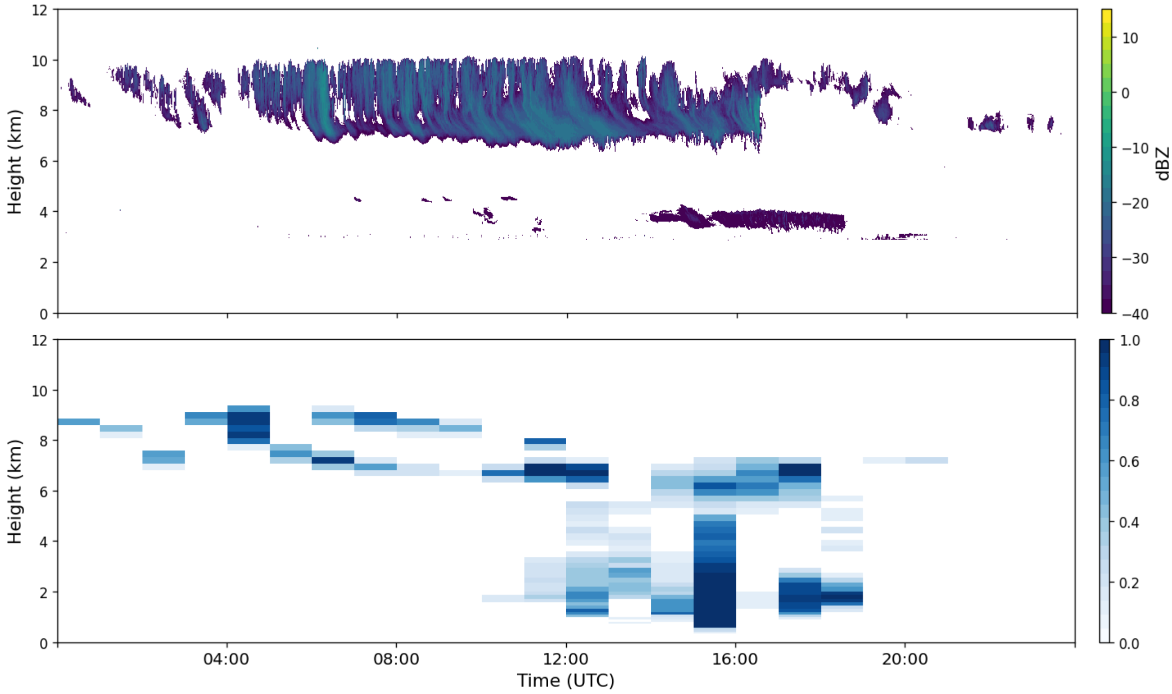

Figure 30, Time-height cross-section of radar reflectivity (upper panel) and model cloud fraction (lower panel) at Schneefernerhaus on 22 April 2022. Taken from Cloudnet.

during the specified time frame. The lower plot shows relative humidity (w.r.t. ice) and temperature on the y-axis. Here, the line illustrates the increase in relative humidity over time as the parcel ascends at the same updraft velocity. The relative humidity was calculated using an average lapse rate derived from the model temperature profile, starting from the parcel's initial height up to 500 meters above.

The air parcel starts at a height of ~8000 m, a temperature of around –38°C and a relative humidity of ~95 %. The relative humidity threshold for heterogeneous nucleation on mineral dust aerosol of 120% (Ansmann et al. 2025, marked by the dashed orange line), in this case would be reached after just ~175 meters of lofting or 515 seconds, respectively, corresponding to an increase of ~ 25 % in relative humidity. In contrast, almost twice as much lifting would be required to reach a supersaturation of 140%, which is considered the minimum threshold for homogeneous nucleation (Ansmann et al. 2025; Pruppacher and Klett 1997). As the supersaturation decreases after the onset on heterogeneous nucleation in high aerosol loads, the lofting height required for homogeneous nucleation would increase even further, making it an unlikely ice formation path in the observed case. A comparison of INP and ICNC values of the observed dusty cirrus cases to typical values of heterogeneously and homogeneously formed cirrus clouds would be helpful to identify the primary formation pathway. However, no suitable measurements were available for the chosen dates and location. Considering that the vertical resolution of the IFS model at an

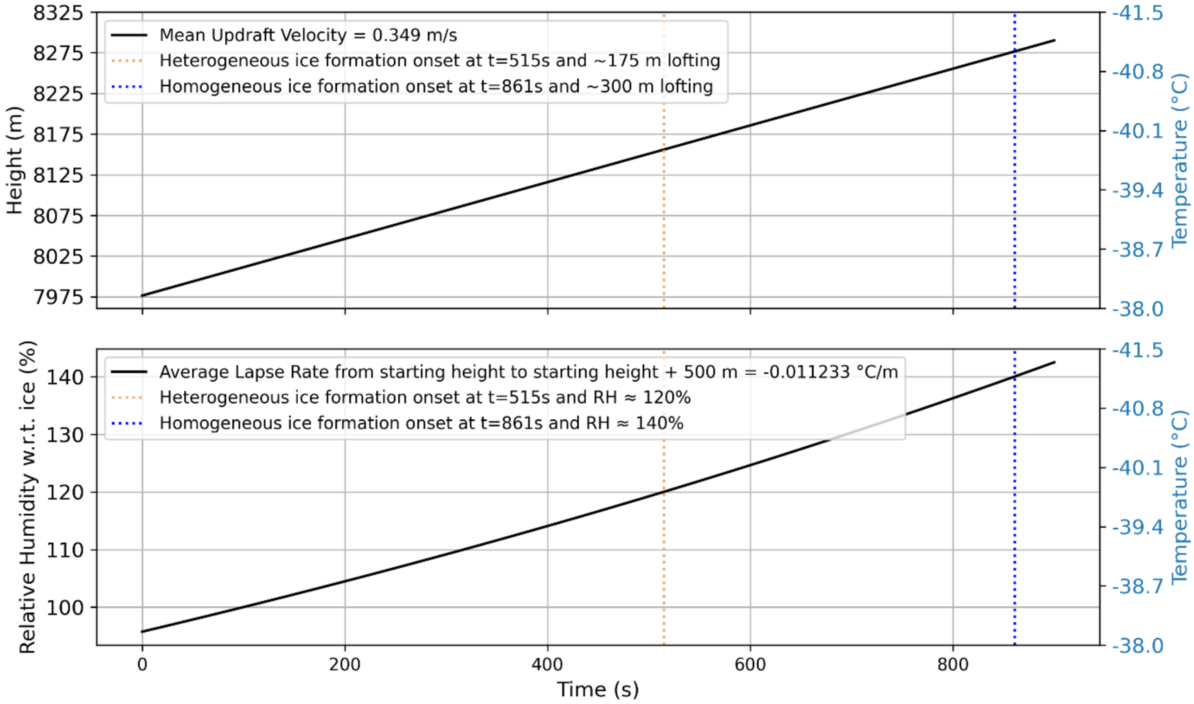

Figure 31, Lofting and relative humidity (w.r.t. ice) required for heterogeneous ice nucleation at an average updraft velocity of 0.349 m/s for the modelled cirrus gap between 14:00 and 15:00 UTC at Schneefernerhaus on 22 April 2022. Calculated from Cloudnet data.

altitude of 8000 m is approximately 300 m, it is likely that such small-scale lofting processes which are already sufficient to reach the supersaturations required for heterogeneous formation of cirrus under high aerosol conditions, cannot be sufficiently captured by the model.

6 Summary, Conclusions and Outlook

6.1 Summary

In the presented master's thesis, the statistical correlation between dust, cirrus formation, and turbulence has been studied using a combination of ground-based height-resolved remote sensing and NWP model data. For detailed information about cloud structure, turbulence, cloud cover, and atmospheric parameters (temperature, relative humidity, wind speed, and direction) a yearlong dataset from the Cloudnet station at Schneefernerhaus containing observations from radar, lidar, microwave radiometer, and ECMWF – IFS model data has been used. Among the stations considered, the Cloudnet station at Schneefernerhaus offered the optimal balance between relatively high data resolution and a substantial number of observed dusty cirrus cases. Dust concentrations were retrieved from the Copernicus Atmosphere Monitoring Service EAC4 Global Reanalysis product, since lidar-derived dust properties are not available in the presence of clouds.

The Eddy Dissipation Rate (EDR) was calculated based on the cloud radar Doppler velocity to serve as proxy of the cirrus turbulence. The column dust load above -38 °C was used to distinguish between regular and dusty cirrus clouds. Daily mean values for EDR and dust load were used to sort the observed cirrus scenarios into low, moderate and high dust as well as low, moderate and high turbulence cases (low: ≤ 15th percentile; moderate: 15th – 85th percentile; high: ≥ 85th percentile, respectively).

A comparison of the EDR distribution for different dust conditions showed that the EDR value with the highest frequency of occurrence was roughly two orders of magnitude higher under high dust load compared to low dust load. No significant correlation between EDR and dust load could be observed in low and moderate dust conditions. However, it is noteworthy that neither cirrus clouds exhibiting high EDR and low dust load nor cirrus clouds with high dust loads and low EDR could be observed. In contrast, a significant linear correlation (R^2 of 0.517) between EDR and dust load could be observed for high dust conditions, suggesting that the presence of dust is likely to contribute to increased turbulence in dusty cirrus clouds.

To assess the influence of other atmospheric parameters on cirrus cloud characteristics and turbulence an analysis of wind shear, relative humidity, and dust concentration was conducted for three representative cases with varying combinations of dust load and EDR.

The results indicate that wind shear and potential associated shear-related turbulence is unlikely to play an important role in the formation of dusty cirrus. Moreover, the cirrus clouds did not form at the interface of a dry, dusty-laden and a moist dust-free air layer as proposed by the mixing instability theory of Seifert et al. (2023) but instead was observed within an air layer that was both moist and dust-laden.

6.2 Answers to the research questions

Based on the presented analysis, the research questions posed in Sect. 3 can be answered as follows:

1. Do turbulent cirrus clouds also appear under dust-free conditions, or is turbulence a characteristic exclusive to cirrus under dust-laden conditions?

This question was addressed in Section 5.2 by examining the correlation between atmospheric dust and turbulence in cirrus clouds. Daily mean EDR values were compared with daily mean column dust load values, integrated from the –38 °C isotherm upward to the lower stratosphere. Analysis of data from the reference year 2022 at Schneefernerhaus revealed no instances of turbulent cirrus clouds — defined as those with EDR values at or above the 85th percentile — coinciding with dust-free conditions (dust load ≤ 15th percentile). Conversely, no cases were found where dust-laden cirrus clouds (dust load ≥ 85th percentile) exhibited low turbulence (EDR ≤ 15th percentile). Combined with a robust correlation between dust load and EDR for high dust load cases ($R^2 = 0{,}517$), these findings suggest a strong association between elevated dust levels and enhanced turbulence in cirrus clouds for cases with a dust load above the 85^{th} percentile. This finding is remarkable, given the location of the measurement site Schneefernerhaus that was selected for this study due to its ideal constellation of high data coverage and quality and high frequency of dust intrusion events. The location of Schneefernerhaus in the Alps Mountains suggests impacts of the pronounced orography on the turbulent structure of clouds. However, this impact seems to be neglectable. Throughout the full year of 2022, high turbulence in cirrus clouds was only observed in presence of high dust loads. Other possible drivers of turbulence in mountainous terrain such as high low-level winds did in no situation lead to EDR values above the 85% percentile.

2. Do the proposed dusty cirrus formation mechanisms agree with state-of-the-art height-resolved observations and models?

The case studies in section 5.3 explore the relationship between different atmospheric parameters. The nighttime radiative cooling theory proposed by Kollath (2010) is primarily based on the analysis of satellite images of dusty cirrus clouds, where the characteristic convective structure appears to dissipate over the course of the day. However, this pattern is not consistently supported by radar observations. In one of the case studies (06.05.2022), no clear decrease in EDR values was observed during daytime. Instead, there was a reduction in the frequency of EDR detections, along with a general decrease in cloud cover. In another case (22.04.2022), the highest EDR values occurred just after sunrise (between 04:30 and 10:00 UTC), followed by a gradual decline of cloud cover as well as EDR throughout the afternoon. In both cases, the highest density of EDR occurrence was observed in regions with the highest dust concentrations. To evaluate the validity of the nighttime radiative cooling hypothesis, a statistical analysis involving a larger sample of dusty cirrus events would be necessary.

The mixing instability theory by Seifert et al. (2023) states that cirrus formation is triggered at the interface between a dry, dust-laden air layer and an overlying supersaturated, dust-free layer. However, during the three presented cases, the atmospheric conditions in the surrounding of the observed cirrus clouds reveal no evidence of such an interface. Instead, the cirrus was only observed to form within a single, supersaturated, dust-laden air mass. The theory assumes that ice nucleation is triggered by upward mixing of dust aerosol into a moist layer. However, the observations suggest that — while the dust remains within the same air mass — turbulence may indeed be responsible for lofting mineral dust to altitudes where supersaturation exceeds the threshold for heterogeneous ice nucleation.

3. What are the atmospheric conditions necessary for "dusty cirrus" and does wind shear play a role in driving the observed turbulence?

The atmospheric conditions necessary for the formation of "dusty cirrus" and the role of wind shear in generating turbulence remain open questions. Seifert et al. (2023) proposed that vertical mixing due to wind shear or gravity waves could loft mineral dust into supersaturated layers, initiating heterogeneous ice nucleation. Their sub-grid parameterization assumes minimum thresholds of 50 µg/kg for dust concentration and an ice supersaturation S_i of 0.7. However, the combination of model and observational data analyzed in this study suggest that dusty cirrus clouds can already form at simulated dust concentrations roughly an order of magnitude lower. Moreover, supersaturations calculated from Cloudnet model data at cirrus level generally exceed $S_i = 0.9$, which is significantly higher than the threshold used in the parameterization. Apart from the role of wind shear as a driver of heterogeneous ice nucleation, it was also investigated as a source of turbulence in dusty cirrus clouds. However, no significant vertical wind shear — neither in speed nor in direction — was detected at cirrus altitudes in the examined cases. Additionally, since cirrus formation consistently occurred within a single, dust-laden layer rather than at the interface between two distinct layers, shear-induced turbulence is unlikely to be a dominant factor in these events. These findings call for a reevaluation of the parameter thresholds and mechanisms assumed in current dusty cirrus parametrizations.

4. What are possible reasons for model inaccuracies in the presence of Saharan dust?

There are different factors that can contribute to model inaccuracies in simulating cirrus clouds in the presence of Saharan dust. While ECMWF – IFS, which is used for ACTRIS Cloudnet products, includes advanced aerosol-cloud interaction schemes, it still operates with monthly mean aerosol climatologies based on CAMS reanalysis data. This neglects the influence of extreme dust concentrations associated with dust-infused baroclinic storms on cloud formation and visibility. Another key limitation is the model's vertical resolution. Observations suggest that in some cases less than 200 meters of vertical lofting would suffice to reach supersaturation thresholds necessary for heterogeneous ice nucleation. Therefore, the vertical resolution of about 300 meters at cirrus levels is insufficient to capture sub-grid processes related to cirrus formation. Additionally, uncertainties in the representation of mineral dust's ice nucleation efficiency and in distinguishing between heterogeneous and homogeneous nucleation pathways still limit the accuracy of nucleation parametrizations. Convective activity appears to be poorly resolved, with thick convective clouds consistently underrepresented across the case studies, which suggests there might be a general problem in modelling vertical air motion. This might limit the models accuracy as lofting is seen as one of the most important factors in ice nucleation (Ansmann et al. 2025; Seifert et al. 2023; Spichtinger 2014). Moreover, the horizontal resolution of the model may be too coarse to resolve small-scale turbulent structures, which satellite observations by Kollath (2010) indicate often occur on scales of ~1 km. Together, these limitations highlight the need for improved sub-grid parametrizations and finer resolution to accurately simulate dusty cirrus formation and associated cloud dynamics.

6.3 Conclusion and Outlook

This study highlights the complexity of dusty cirrus cloud formation and the limitations of both observational and modeling approaches in capturing these phenomena. Below, further aspects regarding the data analysis procedure and potential future perspectives are elaborated on.

Misclassifications of the relationships between dust load and EDR of the observed cirrus cloudswere shown to arise in cases with moderate dust load and high EDR, due to insufficient temporal resolution of the data analysis procedure applied within this study. The dust load was derived as a daily mean. In cases with an increased dust concentration during only some hours of the day, the daily mean dust load could lead to a classification into the moderate dust category. In contrast, in scenarios characterized by high dust load and only moderate EDR, the comparatively low observed turbulence cannot be attributed to a classification error. Notably, in these cases, the highest dust concentrations were observed above the cirrus cloud rather than within the observed cloud, as typically seen in events exhibiting both high EDR and high dust load. A further source of uncertainty stems from the reliance on simulated dust concentrations. This was necessary due to the limited availability of lidar observations at cirrus level in dusty cirrus cases. On the one hand, lidar signals are often attenuated by lower-level cloud layers. On the other hand, once a cirrus cloud has formed, the presence and concentration of mineral dust particles can no longer be detected by the lidar. An extensive search of datasets from across Europe was conducted to identify cases in which desert dust aerosol was still visibly detected prior to the formation of cirrus clouds. However, no suitable cases were found.

Nonetheless, the statistical analysis yielded valuable insights into the correlation between dust and cirrus turbulence. Applying the proposed methodology to additional measurement sites that provide combined lidar–radar datasets could enhance the robustness of the observed correlation and contribute to a deeper understanding of the underlying atmospheric processes. Cloudnet, with its international network of measurement sites, presents a good platform for such an extended analysis. Furthermore, information on dusty cirrus in other regions remains scarce — particularly in the outflow of deserts in Central and Eastern Asia and Australia. Remote sensing data from these regions should also be evaluated to expand the understanding of dusty cirrus formation globally. Such investigations might also help to assess the potential influence of mountain ranges (i.e. the Alps) or specific synoptic conditions during Saharan dust transport events on the development of dusty cirrus clouds over central Europe. Besides Cloudnet, satellites such as EarthCARE, Calipso or Cloudsat have the potential to provide a global view on the co-location of cirrus clouds and mineral dust or other aerosol types that can act as INP. To deepen the understanding of the relationship between dust, turbulence and cirrus formation, a synergistic analysis of these satellite observations, particularly from overpasses over ground-based remote-sensing stations, should be performed. Such an approach could provide dust and cloud properties from below and above the cirrus. In this way, the uncertainties caused by signal attenuation could be reduced. Accurate information about the dust concentration at the top of the cirrus cloud is especially valuable, because ice nucleation is most likely to initiate where temperatures are lowest and supersaturations highest. The combination of these observational datasets with model simulations of cloud coverage could further help to identify regions where aerosol-induced cirrus clouds are systematically underrepresented, potentially revealing hotspots of such effects on a global scale. Finally, long term observational datasets from the source regions of the dust would allow observations of freshly formed dusty cirrus before the airmass ages in its transit to central Europe.

The differences between observed and model cloud fraction under dusty conditions were investigated by simulating the updraft for a case where cirrus could be observed but not simulated by the ECMWF − IFS model. The lofting required for an air parcel to reach the supersaturation threshold for heterogeneous ice nucleation on mineral dust was evaluated based on the thermodynamic conditions of the respective case. The analysis demonstrated that sub-grid turbulence could already be sufficient to initiate cirrus cloud formation under the given conditions. While the vertical model resolution at cirrus height is approximately 300 meters, an ascent of just 200 meters would lead to sufficient supersaturation, which could be one reason why NWP models still struggle to simulate dusty cirrus clouds. Higher-resolved model simulations could help address this issue. It appears that vertical, rather than horizontal, resolution is the limiting factor. A vertical resolution on the order of 50 meters at cirrus level may allow for a more realistic representation of lofting-related dusty cirrus formation. However, assessing the practical applicability of such an approach is beyond the scope of this study.

Model-based dust retrievals are constrained by coarse vertical and temporal resolution, whereas height-resolved ground-based remote sensing offers significantly higher-resolution observations. However, such observations can be limited by signal attenuation in the presence of clouds. To improve the understanding of dusty cirrus cloud formation, retrievals of key microphysical properties—such as ice crystal number concentration (ICNC) and size distribution—are essential. These parameters offer critical insights into the dominant ice nucleation mechanism, as ice crystal characteristics differ significantly between homogeneous and heterogeneous nucleation. In this context, INPC–ICNC closure studies using lidar–radar synergy, such as those conducted by Ansmann et al. (2019) and Ansmann et al. (2025) can yield valuable information on the prevailing ice formation pathways under the influence of various aerosol types, including mineral dust and wildfire smoke.

List of abbreviations

ACTRIS – Aerosol, Clouds and Trace gases Research Infrastructure

AWI – Alfred Wegener Institut

CCN – Cloud Condensation Nuclei

CCT – Cirrus Cloud Thinning

COSMO-MUSCAT – Consortium for small Scale Modelling - MUltiScale Chemistry Aerosol Transport

CAMS – Copernicus Atmosphere Monitoring Service

DIBS – Dust-Infused Baroclinic Storm

DKRZ – German Climate Computing Centre

DWD – German Weather Service

EAC4 – ECMWF Atmospheric Composition Reanalysis 4

ECMWF – European Center for Medium Range Weather Forecasts

ECMWF – IFS – European Center for Medium Range Weather Forecasts – Integrated Forecasting System

ECWAM – European Centre Wave Model

Flake – Freshwater Lake model

HTESSEL – Hydrology Tiled ECMWF Scheme for Surface Exchanges over Land

ICNC – Ice Crystal Number Concentration

ICON-ART – ICOsahedral Nonhydrostatic model – Aerosol and Trace Gases

IFS – AER – Integrated Forecasting System - Aerosol

INP – Ice Nucleating Particle

INPC – Ice Nucleating Particle Concentration

IR – Infrared

IWC – Ice Water Content

KIT – Karlruhe Institute for Technology

LIM2 – Louvain-la-Neuve Sea Ice Model version 2

MPI-M – Max Planck Institute for Meteorology

MSG-SEVIRI – Meteosat Second Generation – Spinning Enhanced Visible and Infrared Imager

MOSAiC – Multidisciplinary Drifting Observatory for the Study of Artic Climate

NEMO – Nucleus for European Modelling of the Ocean

NWP – Numerical Weather Prediction

n_s – INAS density

n_i – ice number concentration

PCF – Pore Condensation Freezing

s_{ae} – aerosol surface area concentration

S_i – Saturation ratio with respect to ice

T – Temperature

WCB – Warm Conveyor Belt

4D-VAR – 4-Dimensional Variational Data Assimilation

Bibliography

Ansmann, Albert, Cristofer Jimenez, Daniel A. Knopf, et al. 2025. “Impact of Wildfire Smoke on Arctic Cirrus Formation – Part 2: Simulation of MOSAiC 2019–2020 Cases.” *Atmospheric Chemistry and Physics* 25 (9): 4867–84. https://doi.org/10.5194/acp-25-4867-2025.

Ansmann, Albert, Cristofer Jimenez, Johanna Roschke, et al. 2025. “Impact of Wildfire Smoke on Arctic Cirrus Formation – Part 1: Analysis of MOSAiC 2019–2020 Observations.” *Atmospheric Chemistry and Physics* 25 (9): 4847–66. https://doi.org/10.5194/acp-25-4847-2025.

Ansmann, Albert, Rodanthi-Elisavet Mamouri, Johannes Bühl, et al. 2019. “Ice-Nucleating Particle versus Ice Crystal Number Concentrationin Altocumulus and Cirrus Layers Embedded in Saharan Dust:A Closure Study.” *Atmospheric Chemistry and Physics* 19 (23): 15087–115. https://doi.org/10.5194/acp-19-15087-2019.

Ansmann, Albert, and Detlef Müller. 2005. “Lidar and Atmospheric Aerosol Particles.” In *Springer Series in Optical Sciences*. Springer-Verlag. https://doi.org/10.1007/0-387-25101-4_4.

Baars, Holger, Thomas Kanitz, Ronny Engelmann, et al. 2016. “An Overview of the First Decade of Polly^{NET}: An Emerging Network of Automated Raman-Polarization Lidars for Continuous Aerosol Profiling.” *Atmospheric Chemistry and Physics* 16 (8): 5111–37. https://doi.org/10.5194/acp-16-5111-2016.

Borque, Paloma, Edward Luke, and Pavlos Kollias. 2016. “On the Unified Estimation of Turbulence Eddy Dissipation Rate Using Doppler Cloud Radars and Lidars.” *Journal of Geophysical Research: Atmospheres* 121 (10): 5972–89. https://doi.org/10.1002/2015jd024543.

Bühl, Johannes, Patric Seifert, Martin Radenz, Holger Baars, and Albert Ansmann. 2019. “Ice Crystal Number Concentration from Lidar, Cloud Radar and Radar Wind Profiler Measurements.” *Atmospheric Measurement Techniques* 12 (12): 6601–17. https://doi.org/10.5194/amt-12-6601-2019.

Burrows, Susannah M., Christina S. McCluskey, Gavin Cornwell, et al. 2022. “Ice-Nucleating Particles That Impact Clouds and Climate: Observational and Modeling Research Needs.” *Reviews of Geophysics* 60 (2). https://doi.org/10.1029/2021rg000745.

Choobari, O. Alizadeh, P. Zawar-Reza, and A. Sturman. 2014. “The Global Distribution of Mineral Dust and Its Impacts on the Climate System: A Review.” *Atmospheric Research* 138 (March): 152–65. https://doi.org/10.1016/j.atmosres.2013.11.007.

Climate Change 2013 – The Physical Science Basis: Working Group I Contribution to the Fifth Assessment Report of the Intergovernmental Panel on Climate Change. 2014. With Intergovernmental Panel On Climate Change. Cambridge University Press. https://doi.org/10.1017/cbo9781107415324.

David, Robert O., Claudia Marcolli, Jonas Fahrni, et al. 2019. "Pore Condensation and Freezing Is Responsible for Ice Formation below Water Saturation for Porous Particles." *Proceedings of the National Academy of Sciences* 116 (17): 8184–89. https://doi.org/10.1073/pnas.1813647116.

DeMott, Paul J., David C. Rogers, and Sonia M. Kreidenweis. 1997. "The Susceptibility of Ice Formation in Upper Tropospheric Clouds to Insoluble Aerosol Components." *Journal of Geophysical Research: Atmospheres* 102 (D16): 19575–84. https://doi.org/10.1029/97jd01138.

Engelmann, Ronny, Thomas Kanitz, Holger Baars, et al. 2016. "The Automated Multiwavelength Raman Polarization and Water-Vapor Lidar Polly^{XT}: The neXT Generation." *Atmospheric Measurement Techniques* 9 (4): 1767–84. https://doi.org/10.5194/amt-9-1767-2016.

Fabry, Frédéric. 2015. *Radar Meteorology: Principles and Practice*. Cambridge University Press. https://doi.org/10.1017/CBO9781107707405.

Fromm, Michael, George Kablick, and Peter Caffrey. 2016. "Dust-infused Baroclinic Cyclone Storm Clouds: The Evidence, Meteorology, and Some Implications." *Geophysical Research Letters* 43 (24). https://doi.org/10.1002/2016gl071801.

Fusina, F., and P. Spichtinger. 2010. "Cirrus Clouds Triggered by Radiation, a Multiscale Phenomenon." *Atmospheric Chemistry and Physics* 10 (11): 5179–90. https://doi.org/10.5194/acp-10-5179-2010.

Griesche, Hannes. 2016. "Mast-2016-Griesche-Dust_effects_on_cloud_forecast." Master's Thesis, University of Leipzig.

Griesche, Hannes J., Patric Seifert, Albert Ansmann, et al. 2020. "Application of the Shipborne Remote Sensing Supersite OCEANET for Profiling of Arctic Aerosols and Clouds during *Polarstern* Cruise PS106." *Atmospheric Measurement Techniques* 13 (10): 5335–58. https://doi.org/10.5194/amt-13-5335-2020.

Hagen, Martin, Axel Häring, Stefan Kneifel, and Kersten Schmidt. 2022. "Clouds and Precipitation Observed with Radar." In *Science at the Environmental Research Station Schneefernerhaus / Zugspitze*. Bayerisches Staatsministerium für Umwelt und Verbraucherschutz (StMUV). https://elib.dlr.de/190770/.

Hansell, R. A., S. C. Tsay, Q. Ji, et al. 2010. "An Assessment of the Surface Longwave Direct Radiative Effect of Airborne Saharan Dust during the NAMMA Field Campaign." *Journal of the Atmospheric Sciences* 67 (4): 1048–65. https://doi.org/10.1175/2009jas3257.1.

Hogan, Robin J, and Ewan J O'Connor. 2004. *Facilitating Cloud Radar and Lidar Algorithms: The Cloudnet Instrument Synergy/Target Categorization Product*. August 17.

Hoose, C., and O. Möhler. 2012. "Heterogeneous Ice Nucleation on Atmospheric Aerosols: A Review of Results from Laboratory Experiments." *Atmospheric Chemistry and Physics* 12 (20): 9817–54. https://doi.org/10.5194/acp-12-9817-2012.

Illingworth, A. J., R. J. Hogan, E.J. O’Connor, et al. 2007. “Cloudnet.” *Bulletin of the American Meteorological Society* 88 (6): 883–98. https://doi.org/10.1175/bams-88-6-883.

Inness, Antje, Melanie Ades, Anna Agustí-Panareda, et al. 2019. “The CAMS Reanalysis of Atmospheric Composition.” *Atmospheric Chemistry and Physics* 19 (6): 3515–56. https://doi.org/10.5194/acp-19-3515-2019.

Intergovernmental Panel On Climate Change. 2023. *Climate Change 2021 – The Physical Science Basis: Working Group I Contribution to the Sixth Assessment Report of the Intergovernmental Panel on Climate Change*. Cambridge University Press. https://doi.org/10.1017/9781009157896.

Kärcher, B., P. J. DeMott, E. J. Jensen, and J. Y. Harrington. 2022. “Studies on the Competition Between Homogeneous and Heterogeneous Ice Nucleation in Cirrus Formation.” *Journal of Geophysical Research: Atmospheres* 127 (3). https://doi.org/10.1029/2021jd035805.

Kärcher, B., J. Hendricks, and U. Lohmann. 2006. “Physically Based Parameterization of Cirrus Cloud Formation for Use in Global Atmospheric Models.” *Journal of Geophysical Research: Atmospheres* 111 (D1). https://doi.org/10.1029/2005jd006219.

Kärcher, B., and U. Lohmann. 2003. “A Parameterization of Cirrus Cloud Formation: Heterogeneous Freezing.” *Journal of Geophysical Research: Atmospheres* 108 (D14). https://doi.org/10.1029/2002jd003220.

Kärcher, Bernd. 2017. “Cirrus Clouds and Their Response to Anthropogenic Activities.” *Current Climate Change Reports* 3 (1): 45–57. https://doi.org/10.1007/s40641-017-0060-3.

Kärcher, Bernd. 2018. “Formation and Radiative Forcing of Contrail Cirrus.” *Nature Communications* 9 (1). https://doi.org/10.1038/s41467-018-04068-0.

Koehler, K. A., S. M. Kreidenweis, P. J. DeMott, M. D. Petters, A. J. Prenni, and O. Möhler. 2010. “Laboratory Investigations of the Impact of Mineral Dust Aerosol on Cold Cloud Formation.” *Atmospheric Chemistry and Physics* 10 (23): 11955–68. https://doi.org/10.5194/acp-10-11955-2010.

Kollath, Kornel. 2010. *Cellular Convection in Cirrus Clouds as a Possible Effect of Dust Aerosols*.

Kuebbeler, M., U. Lohmann, J. Hendricks, and B. Kärcher. 2014. “Dust Ice Nuclei Effects on Cirrus Clouds.” *Atmospheric Chemistry and Physics* 14 (6): 3027–46. https://doi.org/10.5194/acp-14-3027-2014.

Lynch, David K., ed. 2002. *Cirrus*. Oxford University Press.

Mitchell, David L, and William Finnegan. 2009. “Modification of Cirrus Clouds to Reduce Global Warming.” *Environmental Research Letters* 4 (4): 045102. https://doi.org/10.1088/1748-9326/4/4/045102.

Owens, R, and Tim Hewson. 2018. *ECMWF Forecast User Guide*. https://doi.org/10.21957/M1CS7H.

Phillips, Vaughan T. J., Paul J. DeMott, and Constantin Andronache. 2008. “An Empirical Parameterization of Heterogeneous Ice Nucleation for Multiple Chemical Species of Aerosol.” *Journal of the Atmospheric Sciences* 65 (9): 2757–83. https://doi.org/10.1175/2007jas2546.1.

Pruppacher, Hans R., and James D. Klett. 1997. *Microphysics of Clouds and Precipitation*. 2nd rev. and enl. Ed. Atmospheric and Oceanographic Sciences Library 18. Kluwer Academic Publishers.

Rauber, Robert M., and Stephen William Nesbitt. 2018. *Radar Meteorology: A First Course*. First edition. Advancing Weather and Climate Science Series. John Wiley & Sons.

Rémy, Samuel, Zak Kipling, Johannes Flemming, et al. 2019. “Description and Evaluation of the Tropospheric Aerosol Scheme in the European Centre for Medium-Range Weather Forecasts (ECMWF) Integrated Forecasting System (IFS-AER, Cycle 45R1).” *Geoscientific Model Development* 12 (11): 4627–59. https://doi.org/10.5194/gmd-12-4627-2019.

Rieger, D., M. Bangert, I. Bischoff-Gauss, et al. 2015. “ICON–ART 1.0 – a New Online-Coupled Model System from the Global to Regional Scale.” *Geoscientific Model Development* 8 (6): 1659–76. https://doi.org/10.5194/gmd-8-1659-2015.

Seifert, Axel, Vanessa Bachmann, Florian Filipitsch, et al. 2023. “Aerosol–Cloud–Radiation Interaction during Saharan Dust Episodes: The Dusty Cirrus Puzzle.” *Atmospheric Chemistry and Physics* 23 (11): 6409–30. https://doi.org/10.5194/acp-23-6409-2023.

Seifert, M., J. Ström, R. Krejci, et al. 2003. “In-Situ Observations of Aerosol Particles Remaining from Evaporated Cirrus Crystals: Comparing Clean and Polluted Air Masses.” *Atmospheric Chemistry and Physics* 3 (4): 1037–49. https://doi.org/10.5194/acp-3-1037-2003.

Seifert, P., A. Ansmann, I. Mattis, et al. 2010. “Saharan Dust and Heterogeneous Ice Formation: Eleven Years of Cloud Observations at a Central European EARLINET Site.” *Journal of Geophysical Research: Atmospheres* 115 (D20). https://doi.org/10.1029/2009jd013222.

Spichtinger, Peter. 2014. “Shallow Cirrus Convection – a Source for Ice Supersaturation.” *Tellus A: Dynamic Meteorology and Oceanography* 66 (1): 19937. https://doi.org/10.3402/tellusa.v66.19937.

Tukiainen, Simo, Ewan O’Connor, and Anniina Korpinen. 2020a. “CloudnetPy: A Python Package for Processing Cloud Remote Sensing Data.” *Journal of Open Source Software* 5 (53): 2123. https://doi.org/10.21105/joss.02123.

Tukiainen, Simo, Ewan O’Connor, and Anniina Korpinen. 2020b. “CloudnetPy: A Python Package for Processing Cloud Remote Sensing Data.” *Journal of Open Source Software* 5 (53): 2123. https://doi.org/10.21105/joss.02123.

Ullrich, Romy, Corinna Hoose, Ottmar Möhler, et al. 2017. “A New Ice Nucleation Active Site Parameterization for Desert Dust and Soot.” *Journal of the Atmospheric Sciences* 74 (3): 699–717. https://doi.org/10.1175/jas-d-16-0074.1.

Wandinger, Ulla. 2005. “Introduction to Lidar.” In *Springer Series in Optical Sciences*. Springer-Verlag. https://doi.org/10.1007/0-387-25101-4_1.

Weger, Michael, Bernd Heinold, Christa Engler, et al. 2018. “The Impact of Mineral Dust on Cloud Formation during the Saharan Dust Event in April 2014 over Europe.” *Atmospheric Chemistry and Physics* 18 (23): 17545–72. https://doi.org/10.5194/acp-18-17545-2018.

Zeng, Yi, Minghuai Wang, Chun Zhao, Yannian Zhu, Daniel Rosenfeld, and Kang-En Huang. 2023. “Extremely High Concentrations of Ice Particles in East Asian Dust-Infused Baroclinic Storm (DIBS) Cirrus Shield: Dominant Role of Dust Ice Nucleation Effect.” *Journal of Geophysical Research: Atmospheres* 128 (6). https://doi.org/10.1029/2022jd038034.